5-2012

FURTHER INVESTIGATION ON MAGNETICALLY INDUCED SUBSEQUENT FAULT AND STUDY ON ELECTROMAGNETIC SCATTERING OF OBJECTS BURIED BELOW A RANDOM ROUGH SURFACE

Haiyan Yang
Clemson University, haiyany@clemson.edu

FURTHER INVESTIGATION ON MAGNETICALLY INDUCED SUBSEQUENT FAULT AND STUDY ON ELECTROMAGNETIC SCATTERING OF OBJECTS BURIED BELOW A RANDOM ROUGH SURFACE

A Dissertation
Presented to
The Graduate School of
Clemson University

In Partial Fulfillment
of the Requirements for the Degree
Doctor of Philosophy
Electrical Engineering

---

by
Haiyan Yang
May 2012

Accepted by:
Dr. Xiao-Bang Xu, Committee Chair
Dr. James R. Brannan
Dr. Anthony Q. Martin
Dr. L. Wilson Pearson

ABSTRACT

This dissertation contains two subjects: further development of numerical technique for the analysis of magnetically induced subsequent fault (MISFault) in overhead power lines and its implementation into a software upgrade; and first-phase of study on the electromagnetic scattering from objects buried below a random rough surface making use of the multidomain pseudospectral time domain (PSTD) method and Monte-Carlo simulation.

An initial electric fault can result in strong magnetic torque on the overhead power line conductors, which will make them swing and may bring them to close proximity or in contact with one another, causing a subsequent fault. In Chapter 2, Computer simulations for the analysis of the subsequent fault in transition spans, which are often required in power line topology, are developed. A dynamic analysis of swing movement of power line conductors subsequent to an initial fault is presented to track the smallest distance between the conductors. In Chapter 3, the simulation is implemented into the upgrade of the MISFault analysis software. Its functions are depicted in details. The MISFault software is being used by Duke Energy Company and is expected to be useful to a utility for eliminating the magnetically induced subsequent faults.

The multidomain pseudospectral time domain (PSTD) method has been developed and successfully applied to solve a variety of electromagnetic scattering problems in the past decade. It is a novel algorithm with improvement over traditional

FDTD method. In Chapter 4, a multidomain PSTD algorithm is developed to investigate the scattering from a 2-D cylinder in free space. Sample numerical results are presented and validated. Then, the theoretical derivations are extended for the analysis of scattering from 2-D objects buried below a random rough surface.

DEDICATION

This dissertation is dedicated to my parents, deceased Uncle Li, Hai-xia and, to love.

ACKNOWLEDGMENTS

I would like to sincerely thank my major advisor, Dr. Xu for his invaluable guidance, unswerving support as I am pursuing the degree. This dissertation is not possible without his patience, generosity and encouragements. My gratitude is extended to him and Yihong A Yi for caring for my growth and life through the years.

My sincere gratitude and appreciation go to Dr. Brannon, Dr. Martin and Dr. Pearson for serving on my committee members, sharing their knowledge and for their encouragements. Thank Dr. Martin for advice, the internship opportunity (in memory of Dr. Gordon Love). I appreciate Profs. Q.H. Liu, Y. Chen, Y. Shi and Dr. G.X. Fan for their technical discussions and comments.

Special gratitude goes to the Pearsons, the Herrans, Mrs. Joan Servis and Mr. Jim Jones. I would not have carried on so far if not for their resolute support, steadfast love in many ways. I am truly grateful for Dr. Butler and Dr. Noneaker who have always encouraged and trusted in me; Thank my other friends, near and far, present and departed who have helped me with perseverance throughout this long journey.

Additionally, I appreciate the financial support provided by Duke Energy Co., the Department of ECE at Clemson University and National Science Foundation (ECCS – 0821918).

TABLE OF CONTENTS

Table of Contents (Continued)

LIST OF FIGURES

List of Figures (Continued)

Figure Page

List of Figures (Continued)

Figure Page

LIST OF TABLES

Table Page

CHAPTER 1

INTRODUCTION

The work of this dissertation is composed of two research projects that the author has been involved in. The first one focuses on further development and application of numerical techniques in the analysis of overhead power lines under the influence of strong magnetic field when an initial fault occurs and then the software implementation based on the numerical techniques. The second one is to investigate the electromagnetic scattering from a buried object below a random rough surface.

Recently, the subject of magnetically induced subsequent fault (MISFault) in overhead power lines has drawn attention from power industry and researchers. To identify the probability of the magnetically induced subsequent faults, computer simulations have been developed and are presented in [1] for level spans and in [2] for inclined spans. The computer simulations are based on a dynamic analysis tracing the smallest distance between the power lines as they are swinging after the initial fault occurs, to determine whether or not they would touch each other causing a subsequent fault. However, in practice, a power transmission/distribution line topology may require a transition from one power line structure to another or to a dead end of a circuit. Such a required transition can be realized by a span called *transition* span. Since the transition spans, in addition to level spans and inclined spans, are often used in power line topology, it is also necessary to study the probability of the magnetically induced subsequent fault in transition spans. Therefore, in the next two chapters of this dissertation, a dynamic

analysis, based on fundamental electromagnetics and mechanics, of the swing movement of overhead power line conductors in a transition span subsequent to an initial fault is presented to track the smallest distance between the conductors, which is an important element useful for predicting the probability of the subsequent fault. Then, this analysis is implemented into the upgrading of the MISFault analysis software.

Analysis of electromagnetic scattering of buried objects has been widely used in sensing and remote-sensing applications. Research has been reported on this subject for a buried perfect electric conducting (PEC) sphere [3], for an object above a rough surface [4], [5], for a buried penetrable and/or PEC spheroid [6], [7], and for multiple objects buried beneath a rough surface [8]. In all the works cited above, the earth was assumed to be homogeneous. Meanwhile, the scattering from a 3-D target embedded in a two-layered half-space medium has been investigated using the method of moments (MoM) [9], but the interfaces were assumed to be *flat*. However, in reality, the earth is of layered structure, which adds more complexity to the analysis. As pointed out in [10] and [11], it is important to incorporate the roughness of the interface involved in the scattering because of its significant impact on the scattered signature. In [10], the scattering from two-layered random rough surfaces with and without buried objects has been analyzed using the steepest descent fast multi pole method (SDFMM). This analysis was limited to the case that the depth of the underground interface must be less than one free-space wavelength to satisfy the quasi-planar structure constraint of the SDFMM. In [11], the scattering from a buried cylinder in layered media with rough interfaces has been studied based on extended boundary condition method (EBCM).

In the past, the Monte-Carlo finite difference time domain (FDTD) technique has been used to study the scattering by a random rough surface (without buried objects) [12] and that from a 3-D object *over* a random rough surface [13]. As indicated in [12], in contrast to surface integral equation formulation, the FDTD approach is more effective for modeling inhomogeneous objects and complex geometries, and is less expensive for the analysis of 3-D problems. In addition, either pulsed or CW illumination can be used in the FDTD approach, propagation of both the total and scattered fields can be observed in the time domain. The FDTD approach based on the classical Yee scheme requires a large number of points per wavelength to ensure that it produces acceptable results. However, the FDTD has drawbacks as pointed out in [14] and [15].

Recently, the multidomain pseudospectral time-domain (PSTD) method has been presented for simulations of scattering by objects embedded in lossy media [15] – [17]. The idea of the PSTD method is to use polynomials to express the unknown solution and its spatial derivatives to achieve more accurate representation of the solution as compared with the classical FDTD approach. The multidomain PSTD can deal with complex geometry with a great flexibility. It only requires π cells per minimum wavelength, and has potential for parallel implementations [15]. Therefore, most recently, a research project has been proposed and funded by NSF to develop an efficient numerical technique, based on the multidomain PSTD method, instead of the classical FDTD, for investigating the scattering from 3-D objects buried in a layered structure with random rough surface. In the PSTD-based formulation, the random rough interfaces can be treated by Monte Carlo simulations. This research project is being carried out in the

Applied Electromagnetic Group at Clemson University. In this dissertation, we complete the first part of this multi-year research project. In Chapter 4, a multidomain PSTD algorithm is formulated for investigating the electromagnetic scattering of a 2-D cylinder placed in free space. The formulation is validated by comparing its numerical data with the analytical results. Then, the theoretical formulation is extended for the analysis of a cylinder buried below a random rough surface, in which special attention is paid to the treatment of the random rough surface and a few important issues are addressed.

CHAPTER 2

MAGNETICALLY INDUCED SUBSEQUENT FAULT (MISFAULT) IN A TRANSITION SPAN OF OVERHEAD POWER LINES

1. Introduction

As introduced in Chapter 1, when an electrical fault occurs, the power line conductors briefly carry a fault current, which is much higher than the normal current level, resulting in a much stronger magnetic force and torque exerted on the power line conductors. Under the influence of the magnetic torque, the conductors will start swinging, which may bring them to close proximity or even contact one another, causing a subsequent fault. This subsequent fault condition may be difficult to identify, but will cause reduced service reliability and poor power quality. Being able to predict and eliminate these subsequent faults will be beneficial to a utility. To identify the probability of the magnetically induced subsequent faults, computer simulations have been developed and are presented in [1] for level spans and in [2] for inclined spans. However, in practice, a power transmission/distribution line topology may require a transition from one power line structure to another or to a dead end of a circuit. Such a required transition can be realized by a span called transition span.

As an example of transition spans, a crossarm to vertical construction and a double circuit to single circuit pole used by Duke Energy [18] are shown in Fig. 2.1. From the figures, one observes that the structure of a transition span is much more complex than that of a level span and inclined span. Due to their complex structures, the

analysis of transition spans must address two major challenges. First, different from level spans and inclined spans studied in [1, 2], the swing axes of the three power lines are not parallel to each other, making it difficult to use one single coordinate system to calculate and then trace the smallest distance between the power lines, which is required for determining the probability of the subsequent fault. Second, the smallest distance between two adjacent power line conductors may occur between any two points, not only the lowest points as the cases studied in [1, 2]. To address these challenges, in this research, we first employ a series of coordinate system transformations and establish a common coordinate system, using which we can calculate the distances between the power line conductors as they are swinging after the initial fault occurs. Then, in a dynamic analysis based on fundamental electromagnetic and mechanics, we trace the distances between any two points on the two adjacent conductors during their swing procedure, and then extract the smallest one, from which we can tell whether or not the power line conductors would touch one another, causing a subsequent fault.

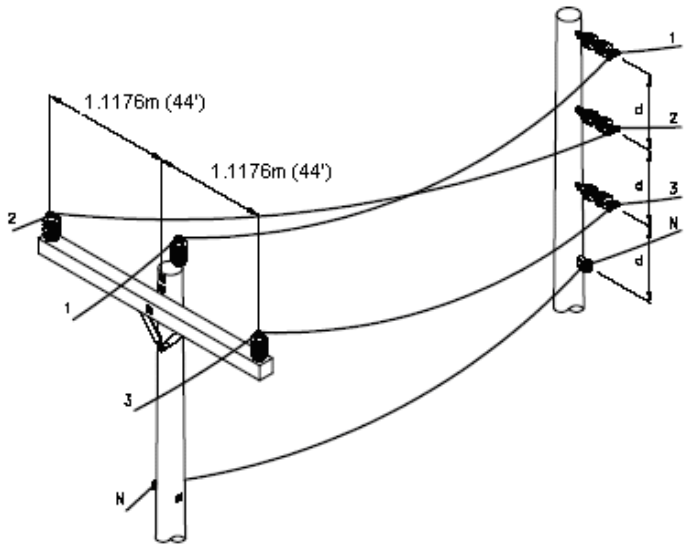

Fig. 2.1 An example of transition span: Crossarm to vertical construction.

2. Coordinate System Transformations

As the first step of the analysis, we make a series of coordinate transformations. The crossarm to vertical construction depicted in Fig. 2.1 is used as an example to illustrate the coordinate transformation procedure. First, we set up a common (*x, y, z*) coordinate system in such a way that its origin *O* is set to be at the center of the top surface of the left pole, the *xz* plane is a horizontal plane parallel to level ground, and the *x*-axis in the *xz* plane is along a line that connects the axes of the two poles. A top view of such established (*x, y, z*) coordinate system is shown in Fig. 2.2, where L_s is the span length. Also, Fig. 2.2 shows three individual coordinate systems (x'_i, y'_i, z'_i) ($i = a, b, c$), each of them is set up for one phase. In each of the three coordinate systems, its origin O'_i is set to be at the lowest point of the phase *i* conductor ($i = a, b, c$) with sag when it is at rest, the $x'_i z'_i$ plane is a horizontal plane parallel to level ground, and the x'_i-axis is formed by the projection in the $x'_i z'_i$ plane of a line connecting the two supporting points of phase *i* conductor. To relate the common coordinate system (*x, y, z*) with each of the three individual coordinate systems (x'_i, y'_i, z'_i), three more coordinate systems (x_i, y_i, z_i) ($i = a, b, c$) are introduced and their top views are also shown in Fig. 2.2. As shown in Fig. 2.2, in each of the three coordinate systems (x_i, y_i, z_i) ($i = a, b, c$), the origin O_i coincides with O'_i, its x_i-axis and z_i-axis are parallel to the *x*-axis and *z*-axis, respectively.

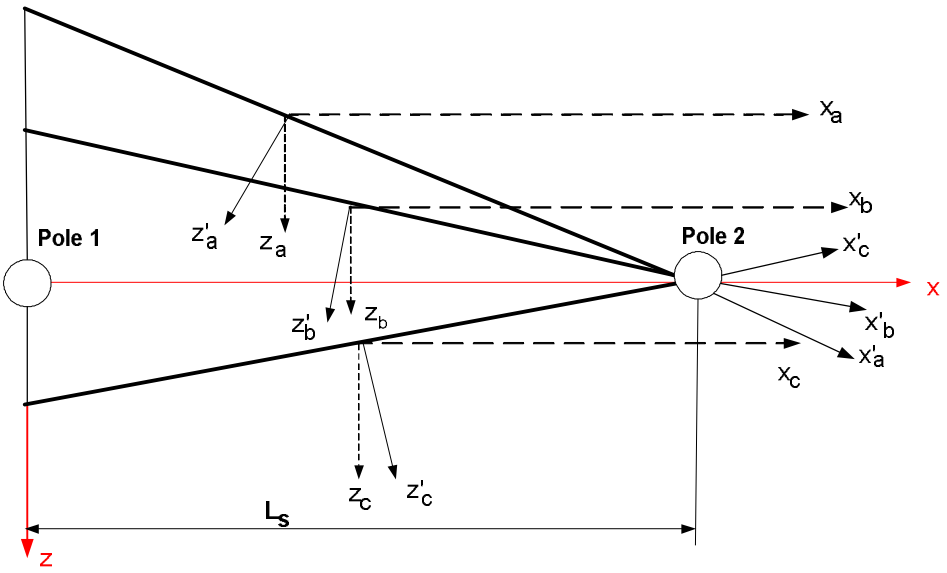

Fig. 2.2 Top view of a complex power line topology.

After setting up these three coordinate systems, we use (x'_a, y'_a, z'_a) and (x_a, y_a, z_a) coordinate systems for phase *a* as an example to illustrate their relationships. As depicted in Fig. 2.3, the (x'_a, y'_a, z'_a) coordinate system can be viewed as a rotation of the (x_a, y_a, z_a) coordinate system by an angle Ψ_a.

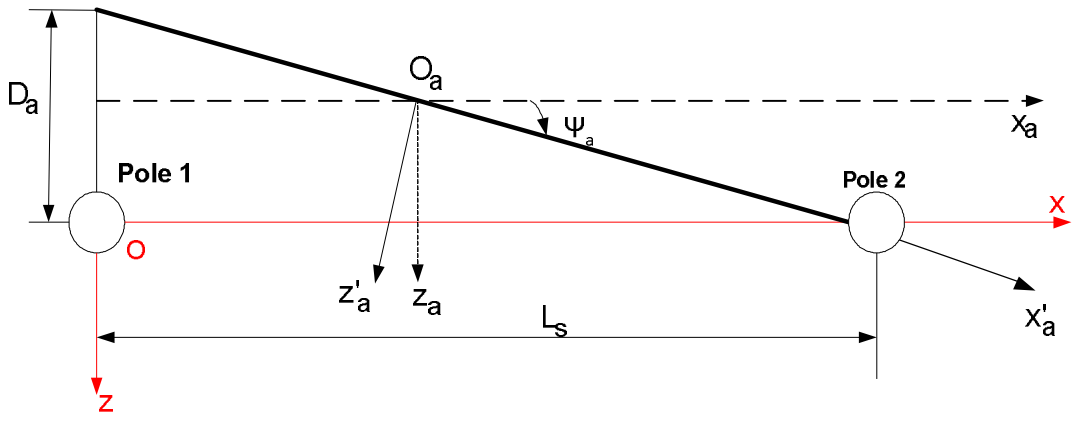

Fig. 2.3 Top view of coordinate transformation for phase a

from ($x_a' y_a' z_a'$) to (xyz) system.

Then, in the (x'_a, y'_a, z'_a) coordinate system, the phase a line can be viewed as an inclined span. As indicated in [2], for an inclined span, the swing axis of the power line conductor would be a line through its supporting points. Therefore, for convenience of a dynamic analysis of the power line swing, we set a new (X_a, Y_a, Z_a) coordinate system in such a way that the X-axis is parallel to the swing axis of the power line as shown in Fig. 2.4. And the new (X_a, Y_a, Z_a) coordinate system can be viewed as a rotation of the (x'_a, y'_a, z'_a) coordinate system by an angle θ_a .

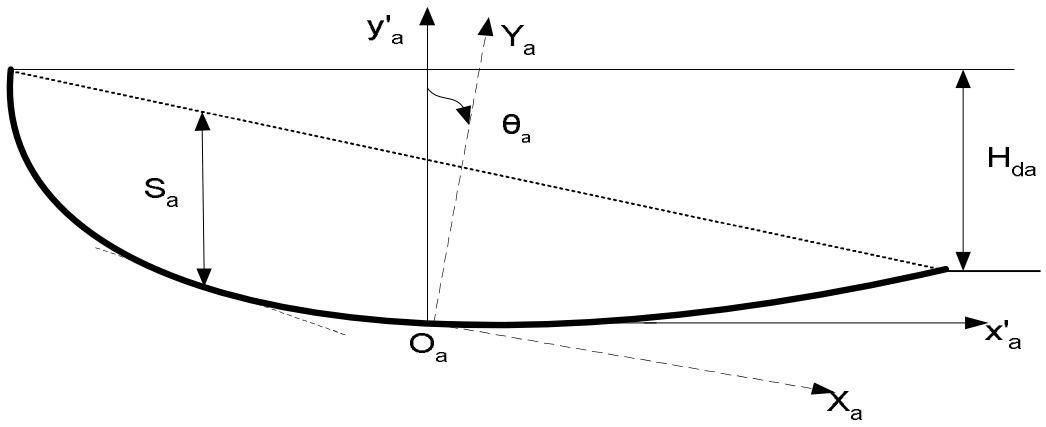

Fig. 2.4 Front view of coordinate transformation for phase a

from ($x_a^{'} y_a^{'} z_a^{'}$) to ($X_a Y_a Z_a$) system.

So far, we have set up three individual coordinate systems (x_i, y_i, z_i), $(x_i^{'}, y_i^{'}, z_i^{'})$, and (X_i, Y_i, Z_i) (i = *a, b, c*) for each phase, as well as the common coordinate system (*x, y, z*). As shown in Figs. 2.2 – 2.4, the first three coordinate systems share the same origin O_i but with different orientations; hence their relationship can be represented by coordinate system rotations. Mathematically, a coordinate system rotation can be performed using a rotation matrix with Euler rotation angles as described in [19, 20], and the rotated coordinate system can be expressed as

$$\begin{bmatrix} X_{rotated} & Y_{rotated} & Z_{rotated} \end{bmatrix} = \begin{bmatrix} X_{old} & Y_{old} & Z_{old} \end{bmatrix} \begin{bmatrix} Rotation & Matrix \end{bmatrix}, \tag{2.1}$$

where $\left[Rotation \quad Matrix \right] = \mathbf{R_x R_y R_z}$, in which $\mathbf{R_x}, \mathbf{R_y}, \mathbf{R_z}$ are for the rotation about *x*-axis, y-axis, z-axis, respectively and are given by

$$\mathbf{R_x} = \begin{bmatrix} 1 & 0 & 0 \\ 0 & \cos\phi & \sin\phi \\ 0 & -\sin\phi & \cos\phi \end{bmatrix}, \quad \mathbf{R_y} = \begin{bmatrix} \cos\psi & 0 & -\sin\psi \\ 0 & 1 & 0 \\ \sin\psi & 0 & \cos\psi \end{bmatrix}, \quad \mathbf{R_z} = \begin{bmatrix} \cos\theta & \sin\theta & 0 \\ -\sin\theta & \cos\theta & 0 \\ 0 & 0 & 1 \end{bmatrix}, \tag{2.2}$$

where φ, ψ and θ are the rotation angles measured clockwise when looking at the origin from a point on the +*x*, +*y* and +*z* axes, respectively. As shown in Figs. 2.2 – 2.4, the rotation from (x_i, y_i, z_i) to $(x_i^{'}, y_i^{'}, z_i^{'})$ system is about *y*-axis at an angle ψ_i measured clockwise; and then from $(x_i^{'}, y_i^{'}, z_i^{'})$ to (X_i, Y_i, Z_i) system is a rotation about *z*-axis at an angle θ_i also measured clockwise. Therefore, making use of equations (2.1) and (2.2) for the coordinate system rotations, we can perform the transformation from (x_i, y_i, z_i) to (X_i, Y_i, Z_i) system and arrive at

$$\begin{bmatrix} X_i \\ Y_i \\ Z_i \end{bmatrix} = \begin{bmatrix} \cos\theta_i \cos\psi_i & -\sin\theta_i & \cos\theta_i \sin\psi_i \\ \sin\theta_i \cos\psi_i & \cos\theta_i & \sin\psi_i \sin\theta_i \\ -\sin\psi_i & 0 & \cos\psi_i \end{bmatrix} \begin{bmatrix} x_i \\ y_i \\ z_i \end{bmatrix}, \tag{2.3}$$

In addition to the transformation from (x_i, y_i, z_i) to (X_i, Y_i, Z_i) coordinate system completed above, the other thing we need to do is to relate the (x_i, y_i, z_i) system to the common coordinate system (*x, y, z*). As illustrated in Figs. 2.2 and 2.3, in these two coordinate systems, the corresponding axes are parallel; the only difference is the locations of their origins O_i and *O*. Such a difference can be determined after several

steps as presented in [21], we obtain the transformation from (x_i, y_i, z_i) to (X_i, Y_i, Z_i) system as

$$\begin{bmatrix} X_i \\ Y_i \\ Z_i \end{bmatrix} = \begin{bmatrix} \cos\theta_i \cos\psi_i & -\sin\theta_i & \cos\theta_i \sin\psi_i \\ \sin\theta_i \cos\psi_i & \cos\theta_i & \sin\psi_i \sin\theta_i \\ -\sin\psi_i & 0 & \cos\psi_i \end{bmatrix} \left[\begin{bmatrix} x \\ y \\ z \end{bmatrix} - \begin{bmatrix} O_{xi} \\ O_{yi} \\ O_{zi} \end{bmatrix} \right], \tag{2.4}$$

or

$$\begin{bmatrix} x \\ y \\ z \end{bmatrix} = \begin{bmatrix} \cos\theta_i \cos\psi_i & \sin\theta_i \cos\psi_i & -\sin\psi_i \\ -\sin\theta_i & \cos\theta_i & 0 \\ \cos\theta_i \sin\psi_i & \sin\psi_i \sin\theta_i & \cos\psi_i \end{bmatrix} \begin{bmatrix} X_i \\ Y_i \\ Z_i \end{bmatrix} + \begin{bmatrix} O_{xi} \\ O_{yi} \\ O_{zi} \end{bmatrix} \tag{2.5}$$

where O_i (i = *a, b, c*) is the location of the origin in the common coordinate system. Equations (2.4) and (2.5) can be used to perform the coordinate system transformations between the (X_i, Y_i, Z_i) (i = *a, b, c*) coordinate and the common (*x, y, z*) coordinate system, which is needed for calculating the smallest distance between the power line conductors and in a dynamic analysis to be presented in the next section.

3. Dynamic analysis on power line swinging caused by an initial fault

When an initial fault occurs, the three-phase power line conductors of a transition span carry a high-level fault current, resulting in a strong magnetic field and magnetic force exerted on the power lines. Under the influence of the magnetic force and the resulting torque, the power lines will start swinging. A dynamic analysis of the power line swinging is presented in this section.

The dynamic analysis of the swinging phase *i* (*i* = *a, b, c*) conductor of a transition span is carried out in the (X_i, Y_i, Z_i) (*i* = *a, b, c*) coordinate system. After the initial fault occurs, the magnetic force exerted on phase *i* power line conductor can be calculated by a line integral along the conductor as

$$\vec{F}_i(t) = I_i(t)\int d\vec{l}_i \times \vec{B}_i(t) \tag{2.6}$$

in which $I_i(t)$ is the current flowing in the phase *i* conductor, $d\vec{l}_i$ is the differential length vector in the direction of the current flow, which is given in Eq. (A3) in the Appendix. Also, in equation (2.6) $\vec{B}_i(t)$ is the magnetic flux density produced by the power line currents, as a function of time *t*. The magnetic flux density $\vec{B}_i$ observed at a point on phase *i* (*i* = *a, b, c*) conductor is produced by the current I_i in itself and the currents I_j $(j = a, b, c, \quad j \neq i)$ in the other two phase conductors, and

$$\vec{B}_i = \vec{B}_{ii} + \sum_j \vec{B}_{ij,i}, \tag{2.7}$$

where $\vec{B}_{ii}$ is due to its own current and can be calculated in the (X_i, Y_i, Z_i) coordinate system as presented in [2]. But $\vec{B}_{ij,i}$ counts the contributions from the other two phase currents and it must be computed in a different way as described below. First, we use Biot-Savart's law to compute the magnetic flux density,

$$\vec{B}_{ij,j} = \frac{\mu_0 I_j}{4\pi}\int \frac{d\vec{l}_j \times \vec{R}_{ij}}{\left|\vec{R}_{ij}\right|^3}, \tag{2.8}$$

where the integral is performed along the phase *j* power line, and $d\vec{l}_j$ is the differential length vector along the phase *j* power line in the (X_j, Y_j, Z_j) coordinate system. Note that such calculated magnetic flux density $\vec{B}_{ij,i}$ is a vector in the (X_j, Y_j, Z_j) coordinate system $(j = a, b, c, \quad j \neq i)$. To make it addable to $\vec{B}_{ii}$ in equation (2.7), we must convert the vector $\vec{B}_{ij,j}$ to a vector $\vec{B}_{ij,i}$ in the (X_i, Y_i, Z_i) coordinate system. Such a conversion can be performed by using vector component transformation twice, the details of which is presented in the Appendix.

To compute the magnetic flux density and then the magnetic force on the power line conductor, it is partitioned into *N* small segments in the (X_i, Y_i, Z_i) (*i = a, b, c*) coordinate system. Each segment is made so small that the magnetic flux density and the magnetic force can be considered as constant over the segment. Note that both $I_i(t)$ and $\vec{B}_i(t)$ appearing in Eq. (2.6) are functions of time, the magnetic force and the resulting torque must vary as functions of time *t* as well when the power lines are swinging. To take the variation into account, we divide the whole swinging procedure into many very short time steps. The duration Δt of each of them is taken to be much shorter than the period T of the *ac* current at power frequency 60 Hz. Within such a short time interval Δt, $I_i(t)$, $\vec{B}_i(t)$ and hence $\vec{F}(t)$ can all be assumed to be invariant as a good approximation. Then, starting from *t = 0* and using a recursive procedure, we can find out the movement of the power lines during each time interval Δt step by step. Finally, the smallest distance between the power lines, as the result of their movement, can be determined, from which

we can predict the probability of the subsequent fault. As shown in Fig. 2.5, after the phase *i* power line (*i*= *a*, *b*, *c*) starts swinging, both the Y_i- and Z_i- component of the magnetic force $\vec{F}_i$, as well as a component of gravity, $mgcos\theta_i$, contribute to the torque $\vec{\tau}$ that makes the power line swing.

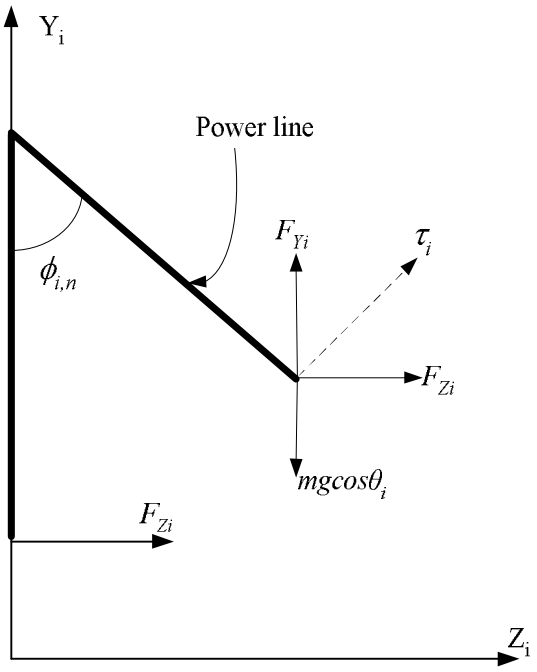

Fig. 2.5 A cross sectional view of the power line phase *i* in motion, the forces and torque exerted on it.

At an arbitrary location after an angular movement $\phi_{i,n}$ of the phase *i* power line conductor, the torque exerted on it can be determined by

$$\tau_{i,n} = \sum_{m=1}^{N} F_{i,n,m} R_{i,m}\,, \tag{2.9}$$

in which $F_{i,n,m}$ is the vector sum of the magnetic force and the gravity exerted on the m^{th} segment of the conductor along its swinging path, and

$$F_{i,n,m} = F_{i,mZ}\cos\phi_{i,n} + (F_{i,mY} - m_m g\cos\theta_i)\sin\phi_{i,n}\,. \tag{2.10}$$

In equation (2.10), $F_{i,mZ}$ and $F_{i,mY}$ are the *Z*- and *Y*- component of the magnetic force $\vec{F}_{i,m}(t)$ on the m^{th} segment of the conductor, which can be calculated by

$$\vec{F}_{i,m}(t) = I_i(t)d\vec{l}_{i,m} \times \vec{B}_{i,m}(t)\,. \tag{2.11}$$

in which $\vec{B}_{i,m}(t)$ is the time-domain expression of the magnetic flux density evaluated at the m^{th} segment centered by $(X_{i,m}, Y_{i,m}, Z_{i,m})$, which can be readily found from its phasor $\vec{B}_{i,m}$. One should notice that after the power lines start swinging, their positions vary as time progresses. Hence, at any specific time, $\vec{B}_{i,m}$ must be re-calculated corresponding to the new locations of the power lines. Then, making use of equation (2.11), we can determine the varying magnetic force $\vec{F}_{i,m}$ exerted on each of the power lines as time progresses.

After obtaining the total torque $\tau_{i,n}$ exerted on the phase *i* power line conductor, we can find out the angular acceleration during its n^{th} angular movement by

$$\beta_{i,n} = \frac{\tau_{i,n}}{I_{i,m}}, \tag{2.12}$$

where $I_{i,m}$ is the moment of inertia of the power line. Then, based on knowledge of the angular acceleration $\beta_{i,n}$, the angular velocity ω_i and the angular movement of the phase *i* power line can be determined by a recursive procedure described below.

When the phase *i* (*i* = *a*, *b*, *c*) power line is at rest (corresponding to $t = 0$,), an arbitrary point on the line is located by $(X_{i,0}, Y_{i,0}, Z_{i,0})$, the initial angular velocity $\omega_{i,0}$ is equal to zero, and the initial angular acceleration is $\beta_{i,0} = \frac{\tau_{i,0}}{I_{i,m}}$, where $\tau_{i,0}$ is the initial torque computed when the power line is at rest. After a short time step Δt, the angular velocity increases to $\omega_{i,1} = \beta_{i,0}\Delta t$ and each of the power lines completes its first angular movement $\Delta\phi_{i,1}$, and

$$\phi_{i,1} = \Delta\phi_{i,1} = \frac{1}{2}\beta_{i,0}\Delta t^2 . \tag{2.13}$$

The angular movement $\phi_{i,1}$ specifies the new location of the power line after Δt, and a point on the line can be expressed by

$$\begin{cases} X_{i,1} = X_{i,0} \\ Y_{i,1} = d_i - (d_i - Y_{i,0})\cos\phi_{i,1} \\ Z_{i,1} = Z_{i,0} + \left(d_i - Y_{i,0}\right)\sin\phi_{i,1} \end{cases} . \tag{2.14}$$

Also, by the end of Δt, the angular acceleration becomes $\beta_{i,1} = \frac{\tau_{i,1}}{I_{i,m}}$, where $\tau_{i,1}$ is the torque computed for the power line at its new location after the first movement. Then, after another time step Δt, the angular velocity further increases to $\omega_{i,2} = \omega_{i,1} + \beta_{i,1}\Delta t$, and the power line completes its angular movement

$$\phi_{i,2} = \Delta\phi_{i,1} + \Delta\phi_{i,2}, \tag{2.15}$$

where

$$\Delta\phi_{i,2} = \omega_{i,1} + \frac{1}{2}\beta_{i,1}\Delta t^2 \quad . \tag{2.16}$$

By the end of $2\Delta t$, the angular acceleration becomes $\beta_{i,2} = \frac{\tau_{i,2}}{I_{i,m}}$, in which $\tau_{i,2}$ is the torque calculated for the power line at its new locations after its second movements. Based on the analysis above, we can formulate the general equations. After *n* time steps $n\Delta t$, the angular velocity is $\omega_{i,n} = \omega_{i,n-1} + \beta_{i,n-1}\Delta t$, and the power line completes its angular movement

$$\phi_{i,n} = \Delta\phi_{i,1} + \Delta\phi_{i,2} + ... + \Delta\phi_{i,n}, \tag{2.17}$$

where

$$\Delta\phi_{i,n} = \omega_{i,n-1} + \frac{1}{2}\beta_{i,n-1}\Delta t^2 . \tag{2.18}$$

The angular movement $\phi_{i,n}$ specifies the new location of the power line at the moment of $n\Delta t$, and a point on the line can be expressed by

$$\begin{cases} X_{i,n} = X_{i,n-1} \\ Y_{i,n} = d_i - (d_i - Y_{i,n-1})\cos\phi_{i,n-1} \\ Z_{i,n} = Z_{i,0} + \left(d_i - Y_{i,n-1}\right)\sin\phi_{i,n-1} \end{cases} . \tag{2.19}$$

At the moment of $n\Delta t$, the angular acceleration of the power line becomes $\beta_{i,n} = \frac{\tau_{i,n}}{I_{i,m}}$, where $\tau_{i,n}$ is the torque calculated for the power lines at their new locations after the n^{th} movement. Then, such calculated $\beta_{i,n}$ is used for the computation of the next movement. This procedure is repeated over a specified time interval of interest, or until two of the power line conductors touch each other. This procedure is repeated over a specified time interval of interest, or until two of the power line conductors touch each other. In this procedure, we need to compare the time consumed $t_n = n\Delta t$ with the duration of the initial fault t_f. The initial fault duration t_f can be determined from the time-current curves of the recloser, corresponding to various fault current levels. Only within t_f, the total force is the sum of the magnetic force due to the fault current and the gravity. After t_f, the magnetic force is negligible and the gravity becomes the major contribution to the torque, which tends to make the power lines to swing back.

Employing the recursive procedure described above, we can determine the possible maximum movement of the power lines and the smallest distance between them,

from which we may predict whether or not the power lines would touch each other, causing a subsequent fault.

4. Results and Discussion

Making use of the computer simulation, based on the coordinate transformations and the dynamic analysis presented above, we study the probability of the magnetically induced subsequent fault in various types of commonly used transition spans. Sample numerical results for a commonly used transition span are presented and analyzed. More results will be presented later in the dissertation.

As the first example, we present the numerical results for line-to-line fault between phase *a* and phase *b* conductors in an intermediate span connecting a *54"*-spacing flat construction on its left side and a *56"*-spacing construction on its right side. It is of span length L_s *= 250'* and sag *s=52"*. The initial fault current is 3447Amperes and the fault duration is 0.26 seconds. The dimensions of such an intermediate span are illustrated in side view and top view in Fig. 2.6. In this figure, a circle is used to represent the horizontal/vertical position of the installation point of each of the three power line conductors on the left and right side of the span. For the purpose of a partial check, we vary the vertical distance *d* and the horizontal distances l_1 and l_2 between the phase conductors on the right side of the intermediate span and study its effect on the numerical results of the smallest distances between the power line conductors summarized in Table 2.1. In part (a) of this table we present the numerical results for this intermediate span

using the actual dimension of a *54"*- spacing flat construction on its left side and that of a *56"*-spacing construction on its right side; then we alter the horizontal distances l_1 and l_2 between the phase conductors on the right side and show the corresponding results in part (b); finally in part (c), we change both the horizontal distances l_1 and l_2 and the vertical distance d in the right-side construction to make it the same as the left side structure, so that the span becomes a level span; the numerical results of which can be compared with that presented in part (d) of this table, obtained using the computer codes for level spans [1]. From the comparison, one observes that as the dimension of the right-side construction gradually reduces to be the same as that on the left-side structure, that is, the intermediate span is changed to a level span, the numerical results of the smallest distances between the power line conductors gradually reduce to be about the same as that obtained from the computer codes for level spans. This is exactly what one would expect, and can be used as a partial check for the computer codes developed for transition spans.

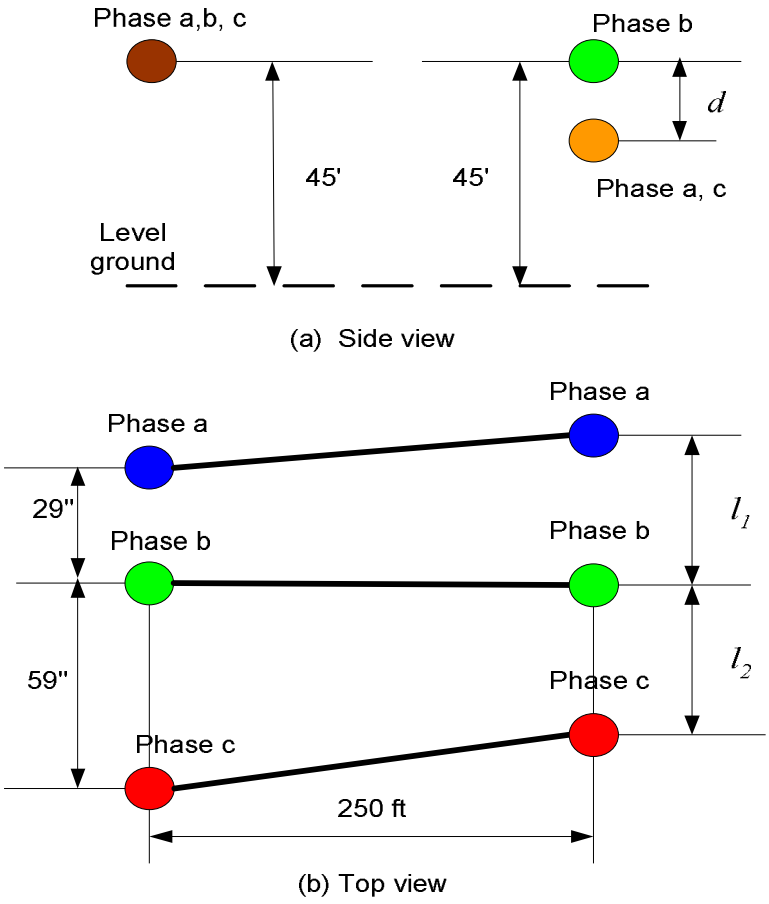

Fig. 2.6 Geometry of an intermediate span.

Table 2.1

The smallest distance between the axes of power conductors when line-to-line fault occurs with 0.26-s initial fault duration at 3447A fault current in an intermediate span with various dimensions of its right-side construction.

Smallest distance between the axes of two power lines (m)	
(a) $l1 = l2$ =1.12m (44"), d = 0.36m (14")	
Phase a - b	0.06102609
Phase b - c	0.6632119
Phase a - c	1.478569
(b) $l1$ = 0.89m (35"), $l2$ = 1.27m (50"), d = 0.36m (14")	
Phase a - b	0.05517985
Phase b - c	0.7106671
Phase a - c	1.396123
(c) $l1$ = 0.74m (29"), $l2$ = 1.50m (59"), d=0	
Phase a - b	0.01664014
Phase b - c	0.6764782
Phase a - c	1.373760
(d) Level span results	
Phase a - b	0.0166264
Phase b - c	0.659232
Phase a - c	1.356055

The sample numerical results presented next are for three-phase fault in a crossarm to vertical construction, depicted in Fig. 2.1, with span length L_s = *255'* and sag *s=52"*. The initial fault current is 3980 Amperes and the fault duration is 0.24 seconds. The dimensions of this transition span are illustrated in Fig. 2.7, where the conductor clearances d_1 and d_2 on the right side are taken to be variable and all the other dimensions are fixed. The smallest distance between the power line conductors, resulting from the magnetically induced subsequent fault, is presented in Table 2.1. From the data shown in

parts (a) – (d) of Table 2.2, one sees that as the conductor clearances d_1 and d_2 vary from *48”* to *38”*, then *28”*, and finally *15”*, the smallest distances between the axes of the power line conductors gradually decrease. In particular, as d_1 and d_2 reduce to *15”*, the smallest distance between the axes of phase *a* and *b* conductors decreases to 0.036 meters, making them almost touch each other. This result makes sense because for the power lines with smaller conductor clearance, they have more chance to touch each other as an initial fault occurs, resulting in higher probability of the subsequent fault.

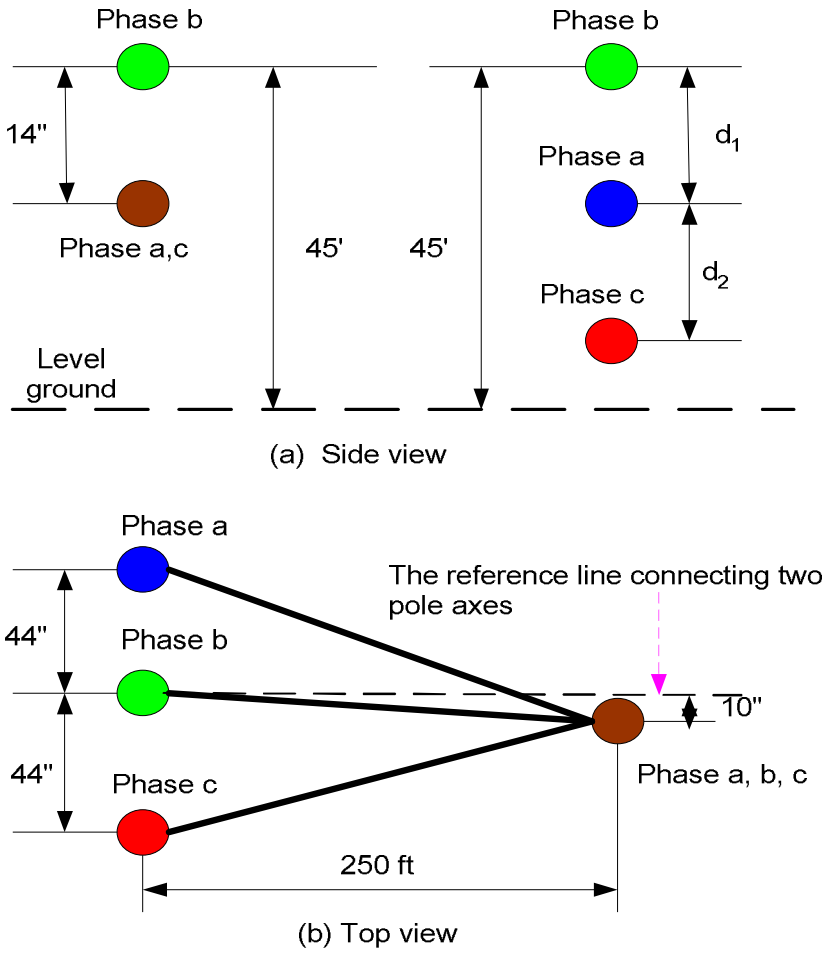

Fig. 2.7. Geometry of a crossarm to vertical construction.

Table 2.2

The smallest distance between the axes of power line conductors when three-phase initial fault occurs in a crossarm to vertical construction with different dimensions of its right-side construction.

Smallest distance between the axes of two power lines (m)	
(e) Conductor clearance $d_1 = d_2 = 1.2$ m (48")	
Phase a - b	0.4856511
Phase b - c	1.007162
Phase a - c	0.6182858
(f) Conductor clearance $d_1 = d_2 = 0.97$ m (38")	
Phase a - b	0.3611948
Phase b - c	0.8795002
Phase a - c	0.4886659
(g) Conductor clearance $d_1 = d_2 = 0.71$ m (28")	
Phase a - b	0.2294606
Phase b - c	0.6728333
Phase a - c	0.3586329
(h) Conductor clearance $d_1 = d_2 = 0.38$ m (15")	
Phase a - b	0.03616398
Phase b - c	0.2432642
Phase a - c	0.1656313

The third example is for three-phase fault in a span guy pole double circuit, the dimensions of which are shown in Fig. 2.8. The initial fault current is 3980 Amperes and the fault duration is 0.24 seconds. The span length is $L_s = 250'$; the sag is taken to be $s=52"$ for all the three phase conductors first, and then the sag of phase *c* conductor is changed to $s_c=40"$ while the sags of phase *a* and *b* conductors remain to be $s_a = s_b=52"$.

The numerical results corresponding to these two cases are presented in part (a) and (b) of Table 2.3, respectively. As shown in this table, for the case that all the three phase conductors are of the same sag, phase *a* and *c* conductors touch each other, causing a subsequent fault. But when the sag of phase *c* conductor is changed to s_c*=40”*, different from that of phase *a* conductor, the power line conductors do not touch. This is because for the case that phase *a* and *c* conductors have different sags, the corresponding points on these two conductors are separated farther, making them more unlikely to touch each other, thus decreasing the probability of subsequent fault.

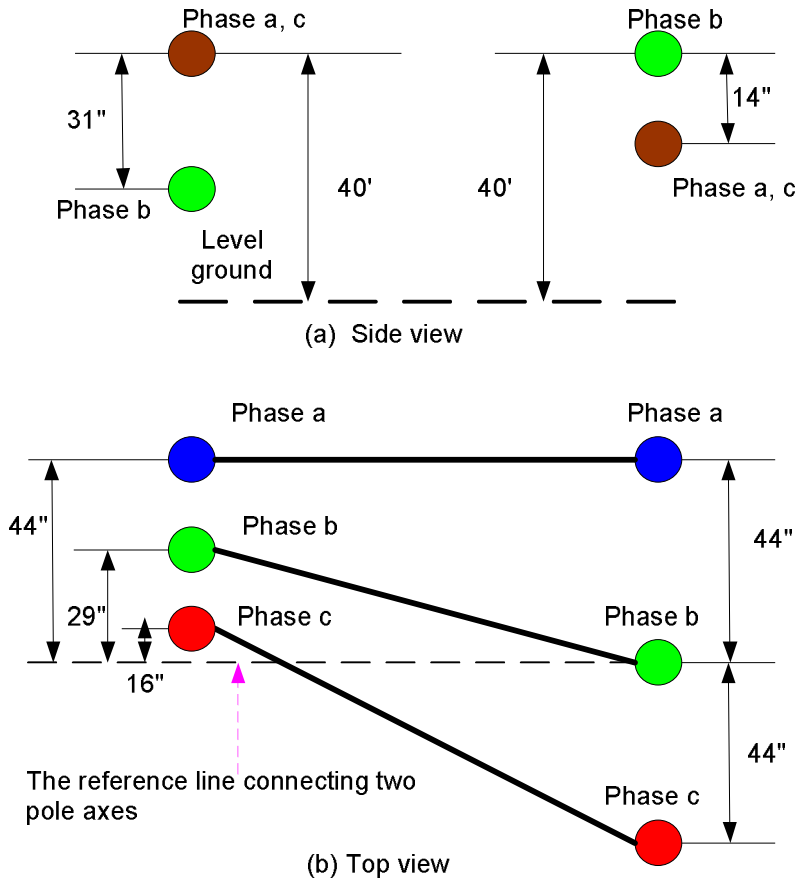

Fig. 2.8 Geometry of a double circuit to single circuit structure.

Table 2.3

The smallest distance between the axes of power conductors when three-phase fault occurs with 0.24-s initial fault duration at 3980.2A fault current in a double circuit to single circuit pole structure with different sags.

Smallest distance between the axes of two power lines (m)	
(a) sa = sb = sc = 1.32m (52”)	
Phase a - b	0.3041216
Phase b - c	0.2945455
Phase a - c	0.01667625 (touch)
(b) sa = sb = 1.32m (52”), sc = 1.02m (40”)	
Phase a - b	0.5676664
Phase b - c	0.2390401
Phase a - c	0.1125081 (no touch)

To check the accuracy of the numerical results, we substitute them into the equation of energy conservation law to see if this equation is satisfied. The energy conservation law requires that the work done by the external force *F* along the movement path of an object must be equal to the sum of the increment of its potential energy and kinetic energy

$$\int \vec{F} \bullet d\vec{s} = mgh + \frac{1}{2}mv^2, \tag{2.20}$$

which is used to check the power line at the moment when the fault currents are cut off. The integral appearing in equation (2.20) is performed along the locus of the power line movement. Also, in equation (2.20), v is the power line swinging velocity, h is its height increment as the result of swinging. A comparison of the work done by the magnetic force and the increment of the total energy of the power line for a typical transition span studied in the third example and presented in Table 2.3 is shown in Table 2.4.

Table 2.4

Comparison of the work done by the magnetic force with increment of energy of the power lines.

Phase	Total work J)	Potential energy (J)	Kinetic energy (J)	Total energy Increment (J)	Relative error (%)
a	27.35	3.60	23.75	27.36	0.017
b	0.001649	0.00164	0.00002	0.001653	0.233
c	27.60	3.77	23.84	27.61	0.0168

From this table one observes that the numerical results well satisfy the energy conservation law. Using Eq. (2.20), all the other cases of the transition spans have been investigated, and the same phenomena are observed.

CHAPTER 3

UPGRADE OF MAGNETICALLY INDUCED SUBSEQUENT FAULT (MISFAULT) ANALYSIS SOFTWARE

1. Introduction

As described in Chapters 1 and 2, an electric initial fault can result in a much stronger magnetic force and torque exerted on the power line conductors, which may cause a subsequent fault. Being able to predict and eliminate these subsequent faults will be beneficial to a utility. Under the sponsorship of Duke Energy Company, computer simulations of the magnetically induced subsequent fault (MISFault) of three-phase power lines has been developed for predicting the probability of the subsequent faults for level spans [1], inclined spans [2], and transition spans [21], and for determining the allowed span length range based on consideration of eliminating the MISFault [22]. Based on the numerical techniques presented in [1, 2, 21, 22], one user-friendly computer software for the analysis of MISFault is developed and upgraded to meet the power quality needs of power industry [23].

The opening screen of the software is shown in Fig. 3.1. It is capable of

(1) predicting the probability of magnetically induced subsequent fault in utility topology for level span, inclined spans, and transition spans.

(2) determining the non-touch span length range/allowed operating span length range from consideration of eliminating the subsequent fault for level spans and inclined spans.

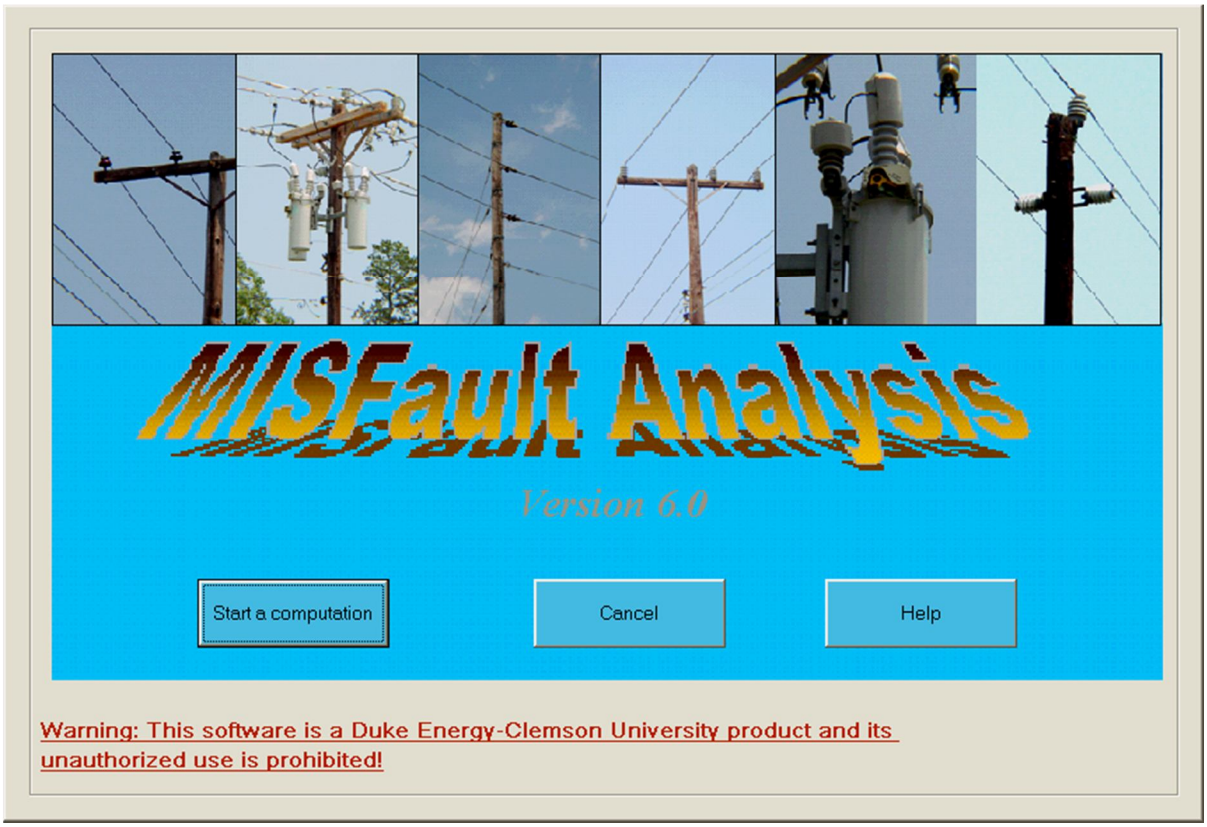

Fig. 3.1 Opening screen of MISFault analysis software.

The software is upgraded to handle a single case or a sequence of multiple case investigations. It has the following modules:

- General options setting;
- Single-case/ Multiple-case mode selection
- Data input

- Structure geometry viewer;
- Pre-test based on the power line structures and its mechanical parameters;
- Computation
- Computation progress viewer;
- Data display and report file creation

In particular, the analysis of magnetically induced subsequent fault *in transit spans*, presented in Chapter 2, is implemented in the upgrading of MISFault software.

2. Upgrade for Transition Span Investigations

A. General settings

The upgraded software can accept single case entry and multiple case scenario entries. After the user clicks the "Start a computation" button on the opening screen, a dialog box (Fig. 3.2) will pop up for the user to choose either single entry or multiple entries, by which a certain command that defines a few different functions, such as different displaying interfaces, will be assigned to the software. In this section, we choose a single case investigation of transition spans as an example to show the functionality of the software. The "General Settings" page for this demonstration is shown in Fig. 3.3.

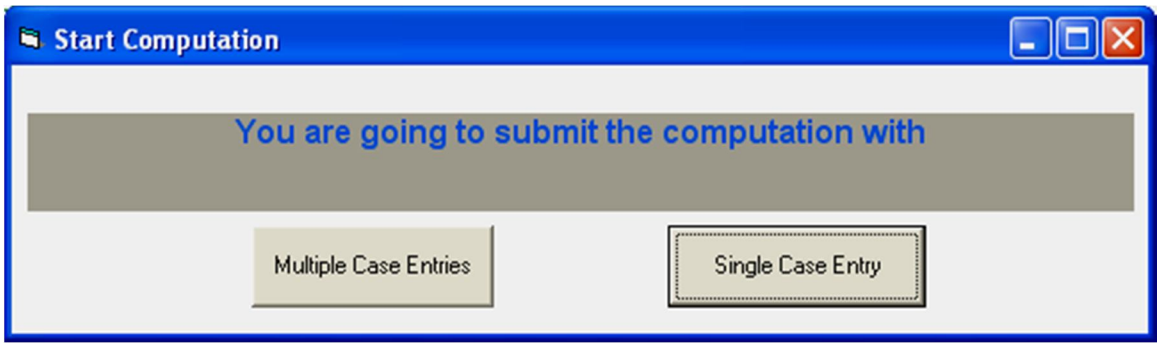

Fig. 3.2 Dialog box for selecting single- or multiple case entries.

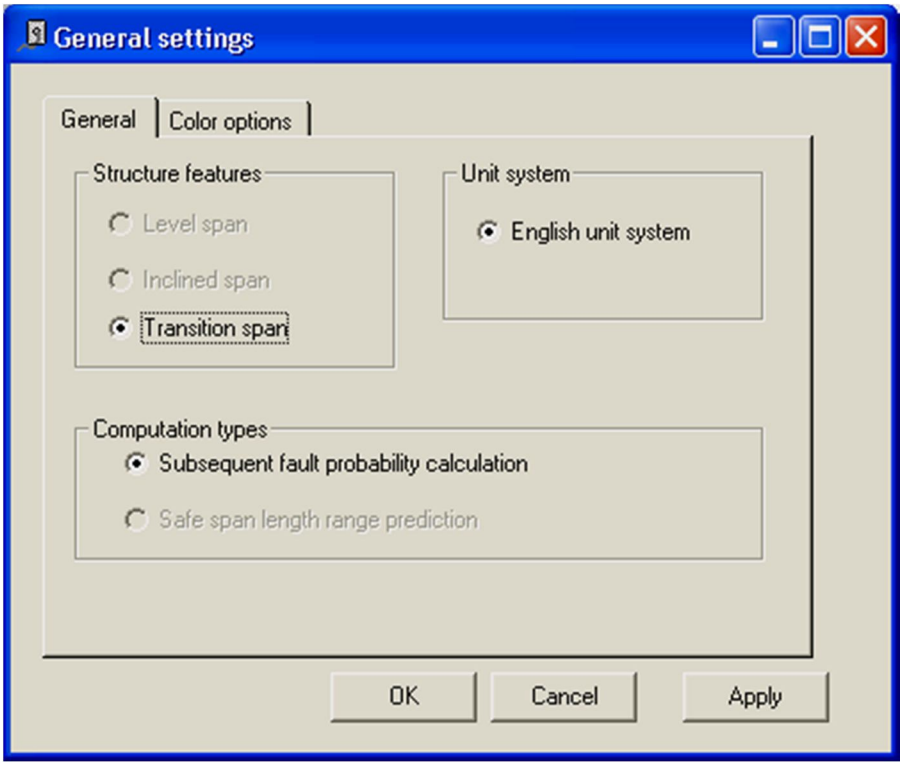

Fig. 3.3 General settings page.

B1. Input for Power Line Structure Geometry

In the initialization page (Fig. 3.4) of the upgraded software, the user can select one of the four types of transition spans framed in “Different Types of Transition Spans” for investigation, and then click the “submit” button. The first three types are typical transition spans listed in the “Primary Line Construction” manual of Duke Energy. The forth one is more general and is to be used to cover the other types of transition spans.

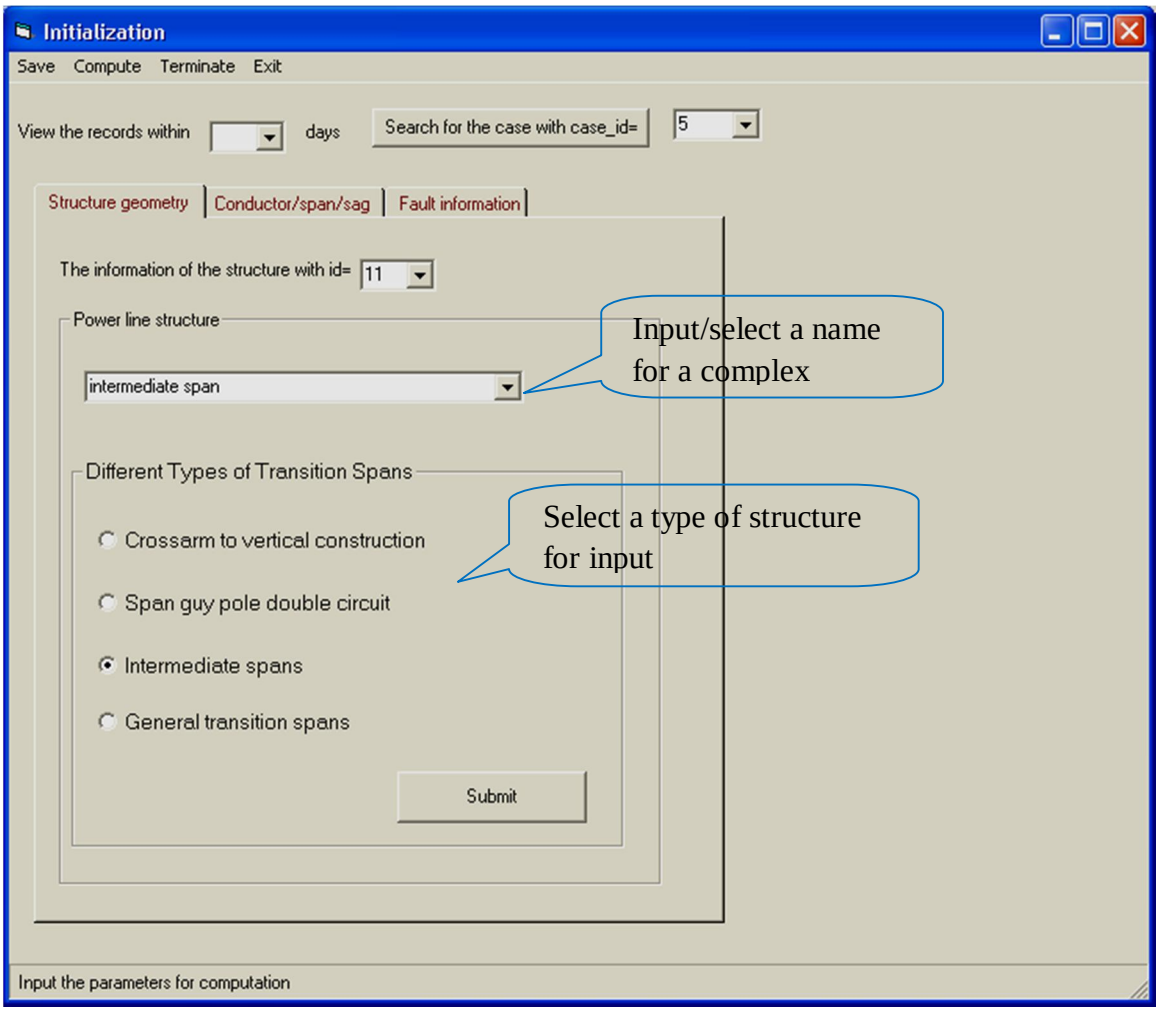

Fig. 3.4 The structure geometry setting for transition span.

If "*Crossarm to vertical construction*" is selected, an input form as shown in Fig. 3.5 will appear. Different from the level span and inclined span, which only need a planar side-view, the transition span structures must be shown in top view and side view to illustrate its complex geometry. In the top/side view, a circle is used to show the horizontal/vertical position of an installation point of each of the three power line conductors on the left and right side of a span. The two circles of the same color on one side (for example, the two green circles on the left side) represent one installation point of a power line conductor in top view and side view. Also, the color of the circles is used to illustrate the line construction of a span, that is, the two circles with the same color on the two sides are actually connected by a power line conductor. The geometry of the transition span can be input to the software by filling out

(1) the text boxes besides the circles for the horizontal/vertical distance between the power lines and their locations relative to the reference lines, which are defined as the local grounds in the side view, and the line connecting the two pole axes in the top view, respectively;

(2) the text box at the most bottom for input of the span length, which must be consistent with the span length input on the span length/sag page;

(3) the text box in the frame of "Ground Inclination" for the height difference between the two ends of a transition span due to the ground inclination, when it is constructed in mountainous areas. The two option boxes embraced in the frame are for the user to select depending on which side, the left side or the right side is higher. The default value of the height difference is zero, which corresponds to level ground.

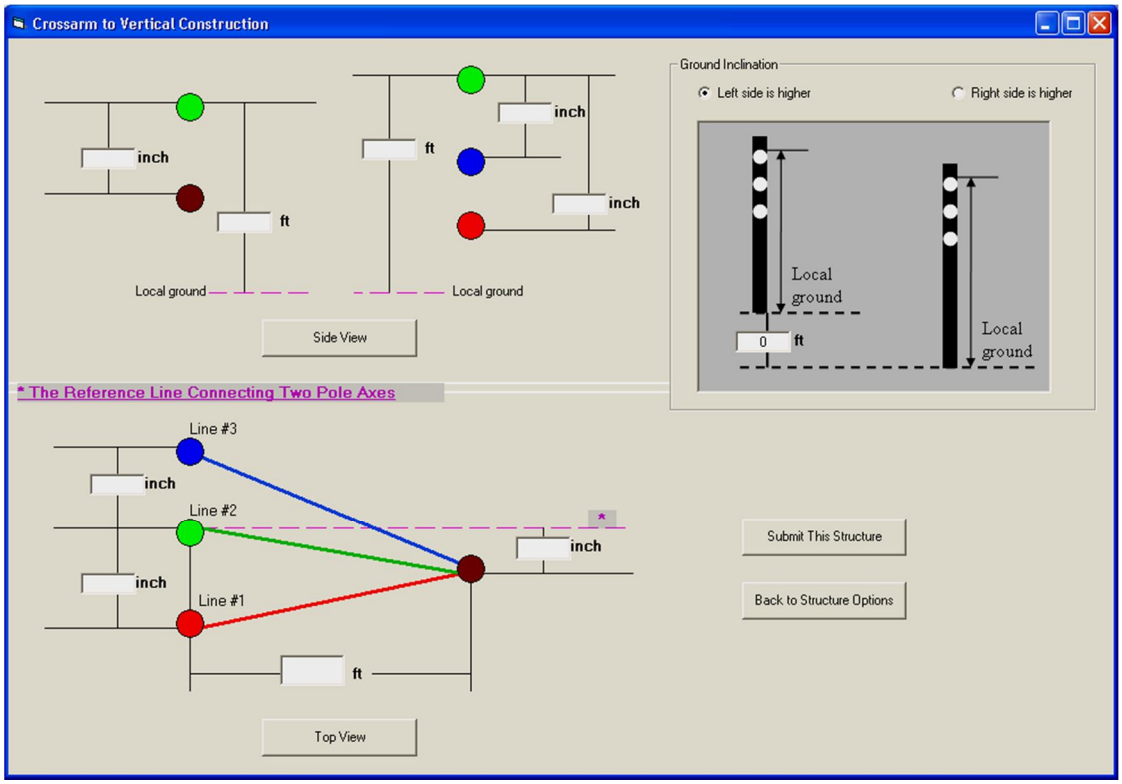

Fig. 3.5 Input form for a transition span from cross arm to vertical construction.

B2. Input for Power Line Conductor/Span Length/Sag Parameters

As shown in the initialization page of Fig. 3.6(a), the user may select the conductor type of the power line to be investigated from a pull-down list, then the diameter and line density of the conductor will appear. Also, in this page, the ambient temperature and the span length can be chosen from the corresponding combo box. Then, select one of the multiple sag values in the combo box of final sag. The upgraded

software can also be used to investigate the power line structures that have different sags. For this case, the user should check “The power lines have different sags” box to enable the input of three different sags in three combo boxes as shown in Fig. 3.6(b).

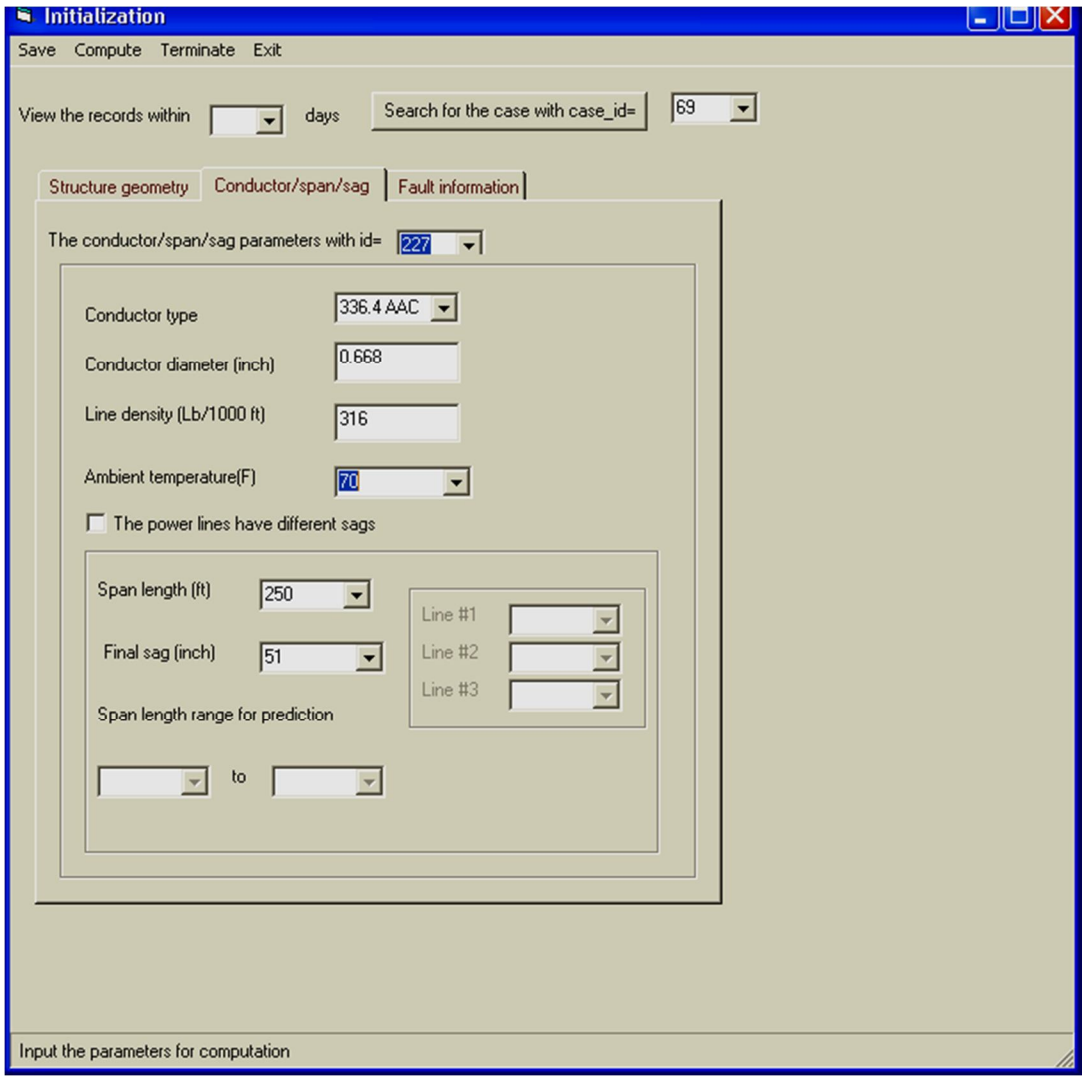

(a)

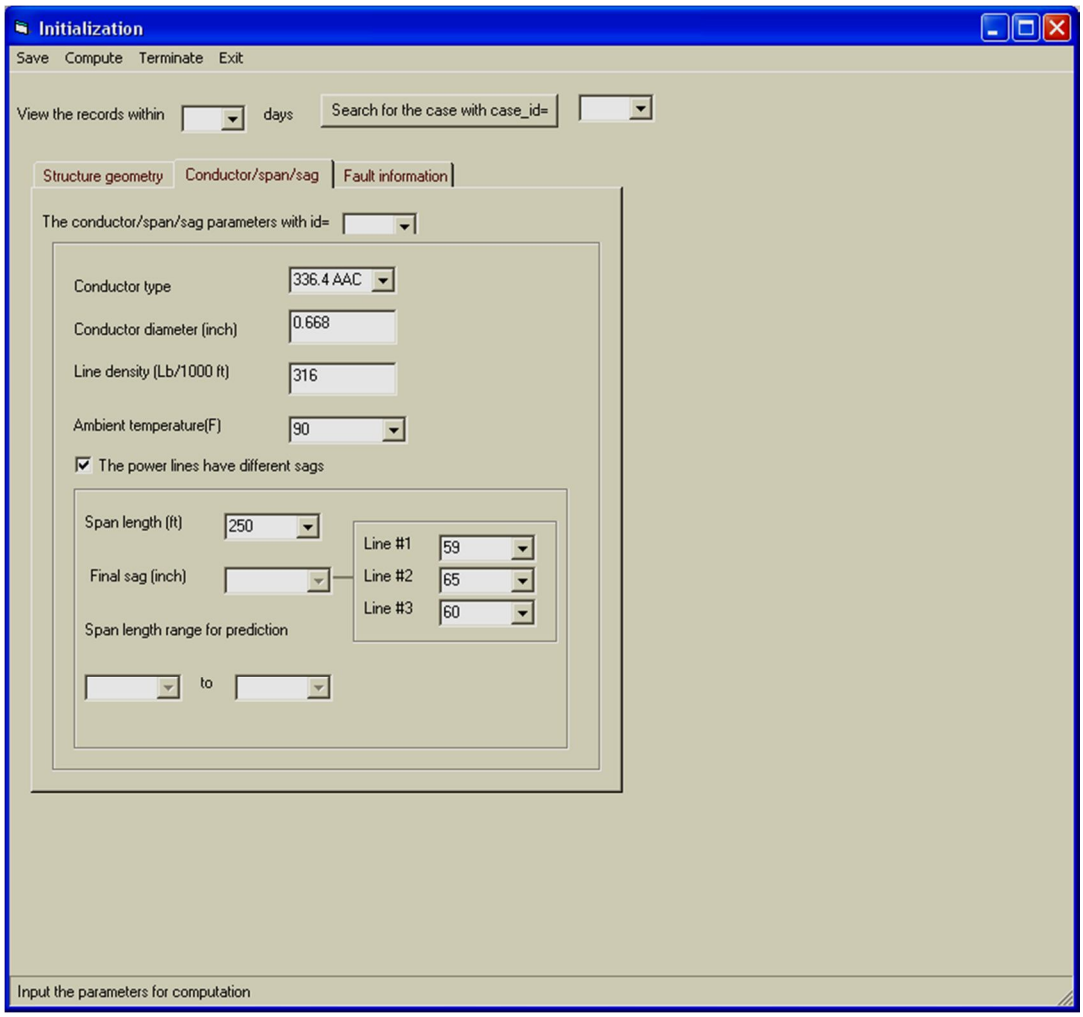

(b)

Fig. 3.6 Initialization page - Conductor/Span/Sag parameters: (a) with the same sags, (b) With different sags.

B3. Input for Initial Fault Information

In the initialization page (Fig. 3.7), the user can click the “Fault information” button; select the fault type to study from a pull-down list, then input the fault duration and the recloser interval, as well as the magnitude of the initial fault currents. After completing all the input and clicking the “Save” button, the input will be checked by the Visual Basic error-capturing scheme. Once any error or invalid input is captured, an error message will be sent to the user and the current process will be suspended until the user corrects the input.

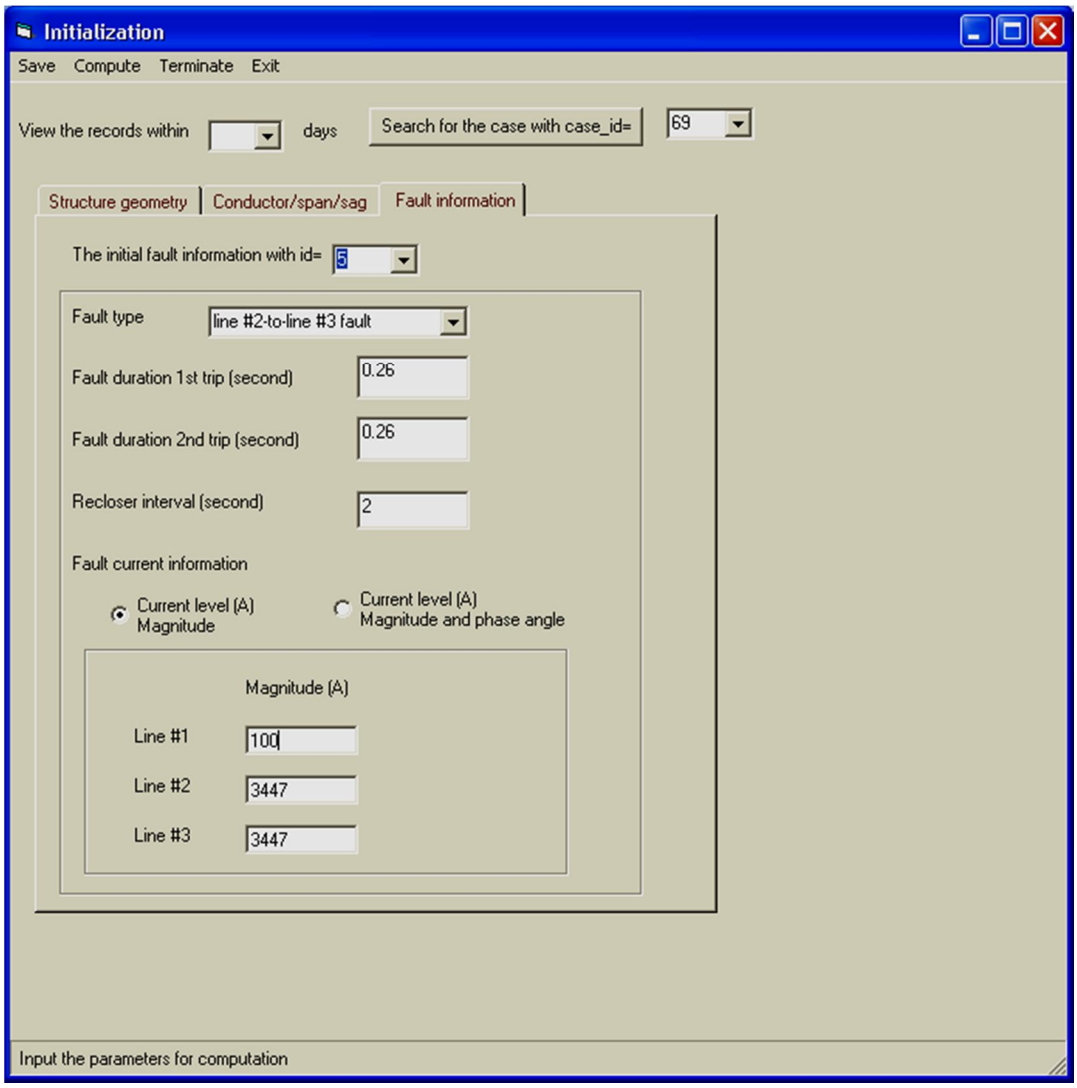

Fig. 3.7 Initialization page - Initial fault information

C. Computation

After the input data are saved and the user clicks the “compute” button from the main menu bar in the initiation page, the upgraded software will start a single-case or a sequence of multiple-case computation. Then, the time when the computation starts will be shown and the progress bar will be activated displaying the

progress of the computation, as shown in Fig. 3.8. When the computation is completed, a message box will pop up informing the user of the completion of the computation. And the data display as well as the report file creation will be activated.

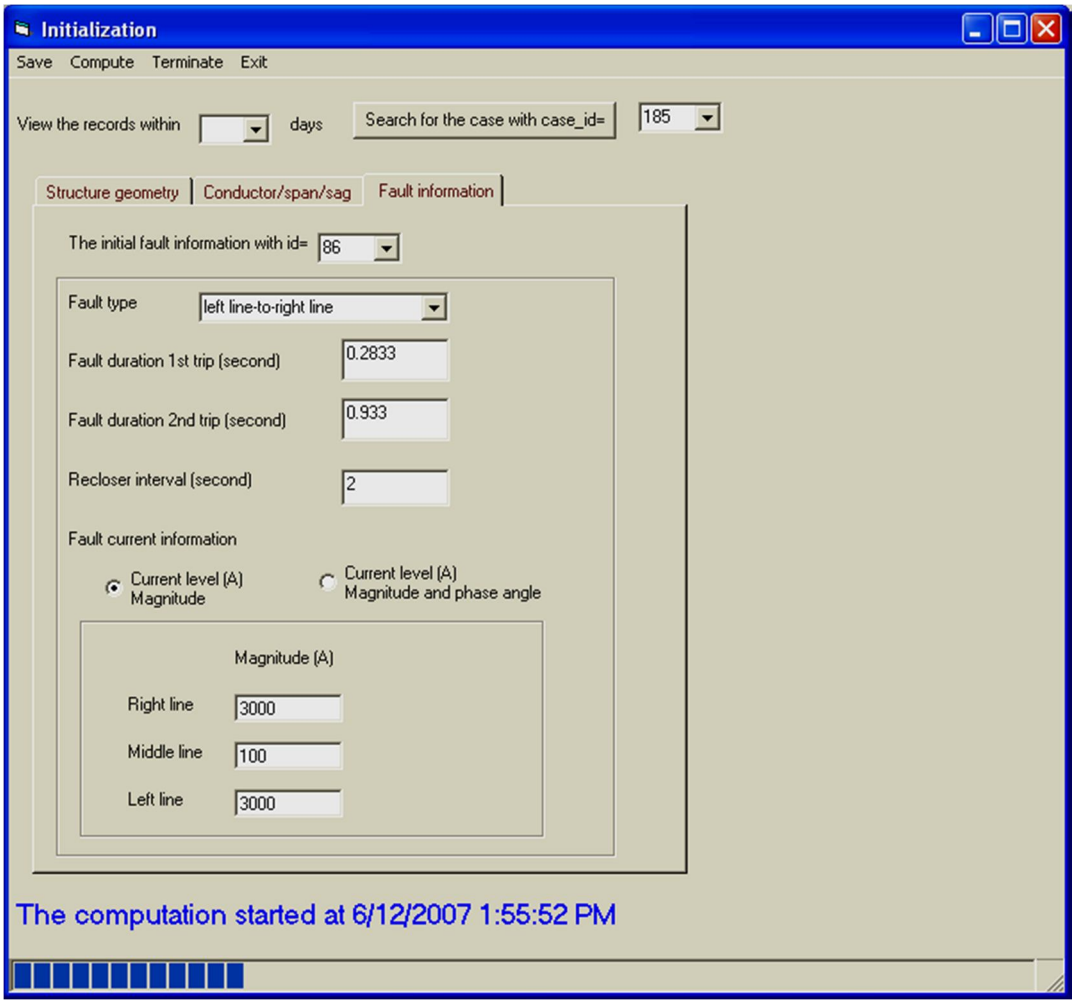

Fig. 3.8 Progress of a single case computation

D. Data Display and Report File Creation

(1) Graphical Display

Going through the same steps as those for level span and inclined spans, the user can view the variation of the *torque* exerted on the power lines of a transition span, the *angular velocities* of the power lines, and the *smallest distance* between their axes with respect to time as they are swinging.

(2) *Report Document*

- Going through the same steps as those for level span and inclined spans, using "Output" or "View", the user may access to the report document and graphical displays for transition spans. A sample report document is displayed in Fig. 3.9.
- To review the structure of the transition span investigated, the user can click the "Structure geometry" in the "View" pull-down menu, then the structure will be displayed in an image form as illustrated in Fig. 3.10, in which the color of the circles is used to illustrate the line construction of a span, that is, the two circles with the same color on the two sides are actually connected by a power line conductor.
- Similar to the other two types of structures, validation of the computation results using the energy conservation law is also available from the "Output" pull-down menu for transition spans.

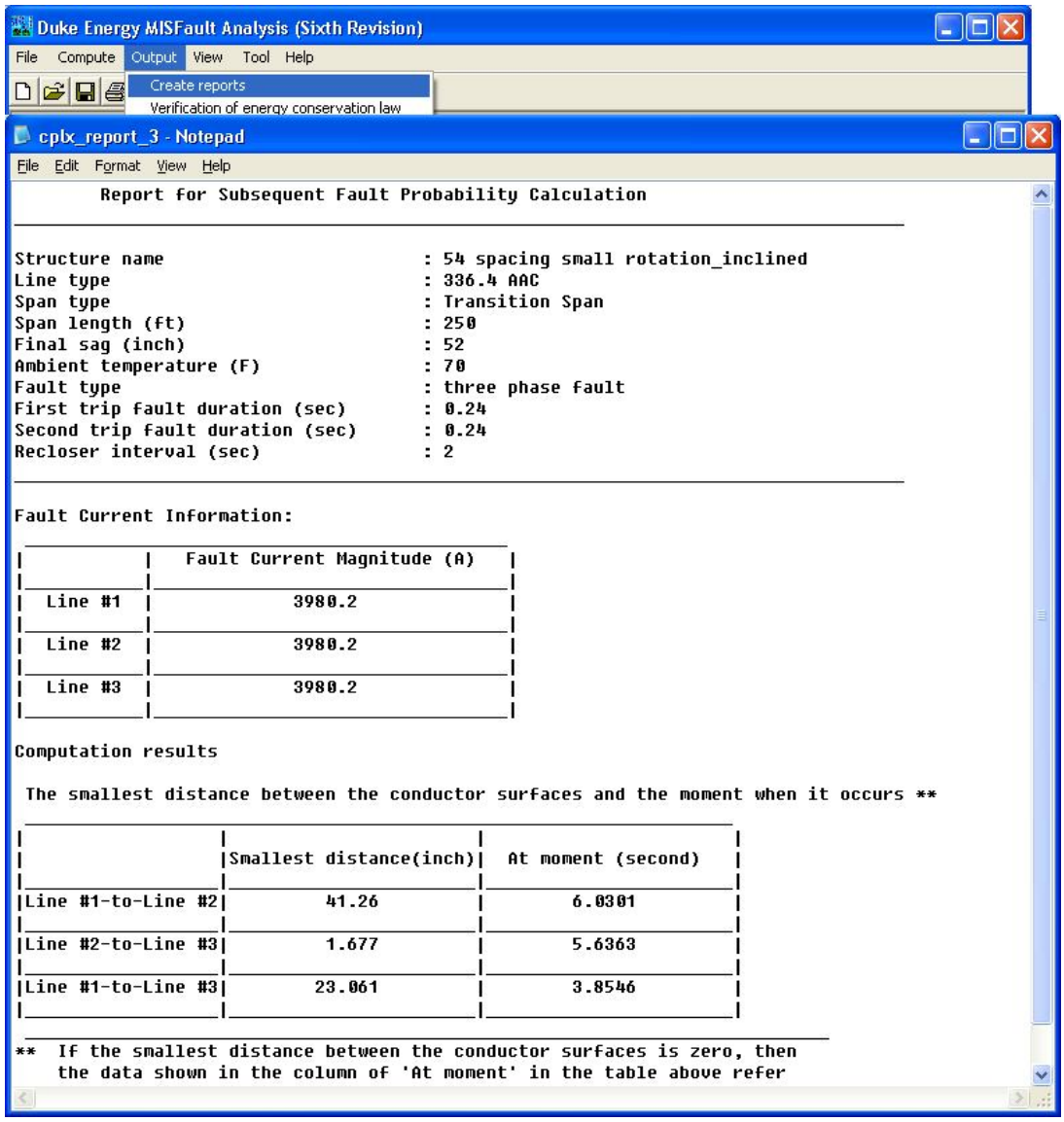

Fig. 3.9 Report document for a transition span.

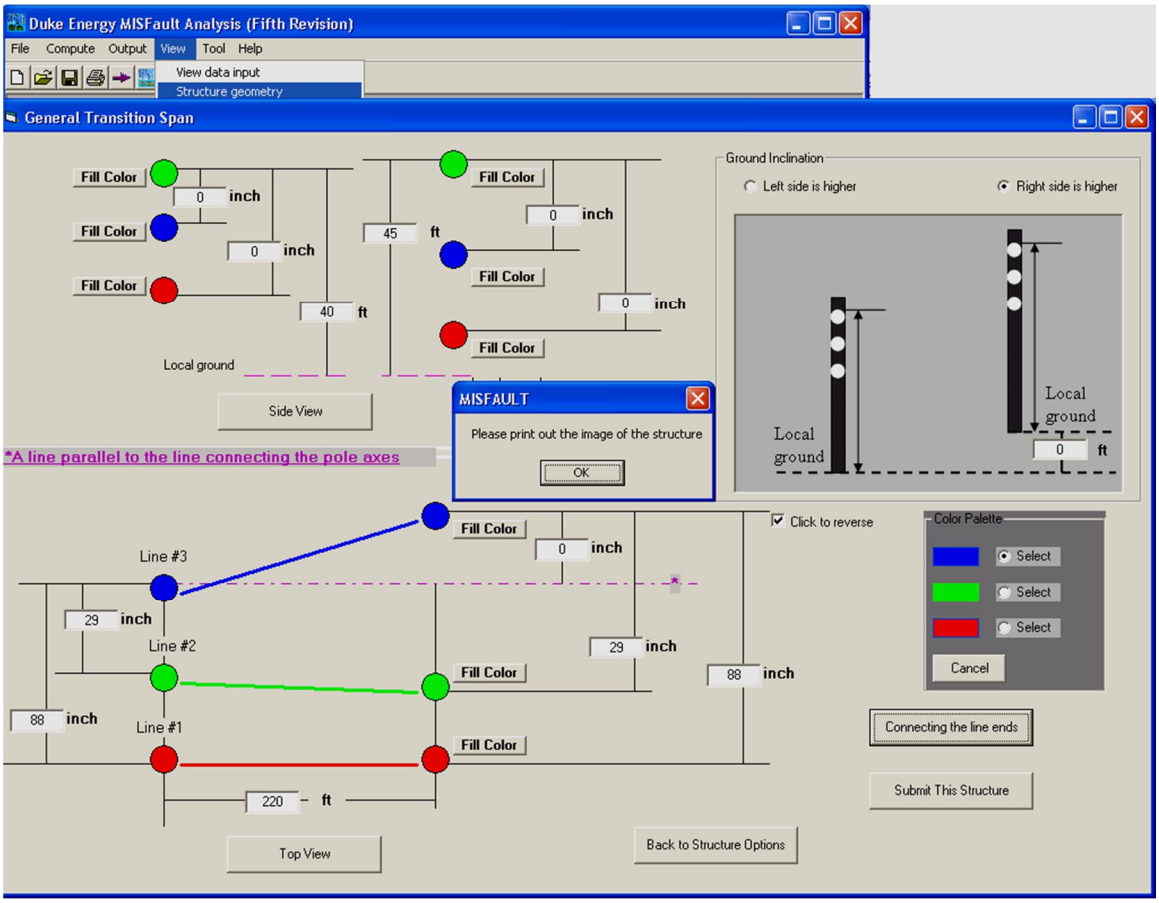

Fig. 3.10 Structure review for a transition span.

In addition to the major modifications mentioned above, the MISFault software is upgraded in other respects to meet the needs of Duke Energy Company [24]. The software is capable of predicting the smallest distance between the power line conductors after an initial fault occurs, from which one can predict the probability of the magnetically induced subsequent fault; and determine the allowed span length range from consideration of eliminating the subsequent fault. It has been tested and the accuracy of

its computation results has been validated by checking with the energy conservation law requirement. It is currently used by Duke Energy for the power quality analysis of overhead transmission/distribution lines and is expected to be useful to a utility for eliminating the magnetically induced subsequent fault.

CHAPTER 4

ELECTROMAGNETIC SCATTERING OF CYLINDER BURIED BELOW A RANDOM ROUGH SURFACE

4.1. Introduction

As the first step of the execution of the NSF-sponsored research project described in Chapter 1, in this chapter, a multidomain pseudospectral time-domain (PSTD) [15][26] algorithm is formulated for investigating the scattering of a two-dimensional (2-D) object placed in free space first. The formulation is validated by comparing its numerical data with the analytical results, for example, the scattering problem from a circular PEC. Then, the theoretical formulation is extended for the analysis of a cylinder buried below a random rough surface, as illustrated in Fig. 4.1. Special attention is paid to the treatment of the random rough surface and a few important issues are addressed.

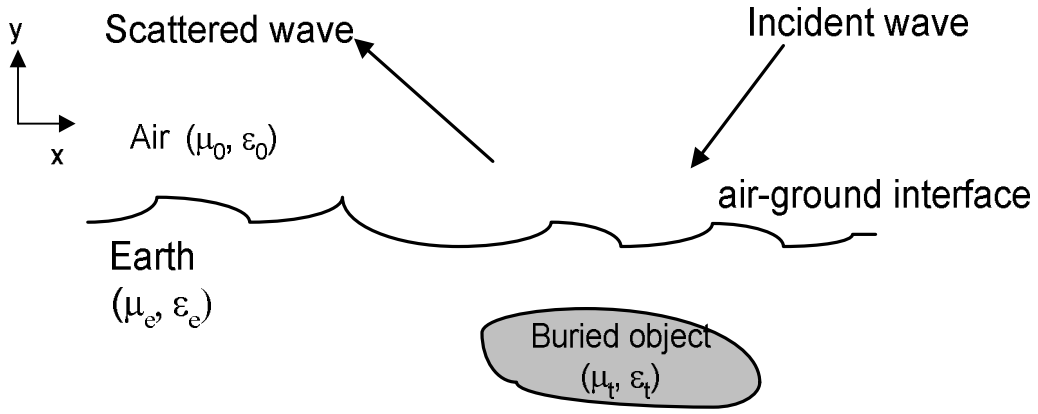

Fig. 4.1 A 2-D object buried below a random rough surface.

The PSTD technique is known as a pseudospectral method used in time-domain, which is formulated on the nodal representations of the spatial derivatives [25]. That is, instead of approximating a function *f(x)* by a series of basis functions in traditional spectral method [28]-[30], it expands the unknown *f(x)* by basis functions $\hat{f}_m$ at a set of fixed grid points ($x_0, x_1, \ldots, x_N$) as

$$f(x) \approx \sum_{m=0}^{N} \hat{f}_m g_m(x), \tag{4.1}$$

where $g_m(x)$ is the Lagrange interpolation polynomial, and

$$g_m(x) = \prod_{i=0, i\neq m}^{N} \frac{(x - x_i)}{(x_m - x_i)}. \tag{4.2}$$

The spatial derivatives are thereby evaluated by

$$\frac{\partial f(x)}{\partial x} \approx \sum_{m=0}^{N} \hat{f}_m \frac{\partial g_m(x)}{\partial x}. \tag{4.3}$$

As pointed out in [26], the Fourier PSTD, which is based on the fast Fourier transform algorithm, is simple to implement and requires only two points per minimum wavelength in homogeneous and smoothly varying inhomogeneous regions; but its accuracy is lower when it is applied to more complex problems. The multidomain PSTD can deal with complex objects with great flexibility, at the cost of slightly increased computational burden since it requires π cells per minimum wavelength [26][27]. Hence, it is employed in this research and its general formulation is presented in the next section. After

validating the multidomain PSTD algorithm formulated through a few numerical examples of the scattering in free space in Section 4.3, we extend the formulation to the analysis of scattering of a cylinder buried below a random rough surface in Section 4.4, where special attention is paid to the treatment of the random rough surface.

4.2. The Multidomain PSTD Algorithm

The general formulation of the multidomain PSTD algorithm is presented in this section. It contains the following major components.

4.2.1. Division of the Computational Domain

The computational domain, for determining the scattering of a 2-D cylinder buried below a random rough surface, is divided into non-overlapping subdomains conforming to the problem geometry, as shown in Fig. 4.2.

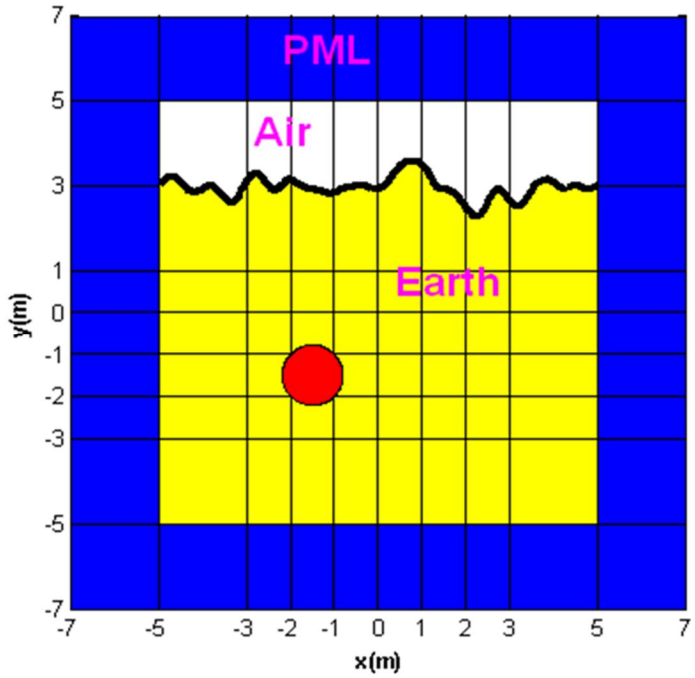

Fig. 4.2 Division of the computational domain into non-overlapping subdomains.

4.2.2 Coordinate Mapping

Each subdomain, which is in general a curved quadrilateral in (x, y) coordinates, is mapped to a unit square ([-1, 1] x [-1, 1]) in (ξ, η) coordinates by means of the coordinate transformation [27] as shown in Fig. 4.3. For a subdomain of rectangular shape, we employ a linear transformation making use of the maxima and minima of x and y as

$$\begin{aligned} x_i &= \left(x_{\max} - x_{\min}\right)\xi_i + 0.5\left(x_{\max} + x_{\min}\right), \\ y_i &= \left(y_{\max} - y_{\min}\right)\eta_j + 0.5\left(y_{\max} + y_{\min}\right). \end{aligned} \tag{4.4}$$

And for a curved quadrilateral, a curvilinear transformation, in terms of Lagrange polynomials based on knowledge of the anchor points, is used. If we denote these anchor points as (x_{pq}, y_{pq}) for $(0 \le p \le P,\ 0 \le q \le Q)$, then

$$x = \sum_{p=0}^{P} \sum_{q=0}^{Q} x_{pq} \phi_p^P(\xi) \phi_q^Q(\eta)$$
$$y = \sum_{p=0}^{P} \sum_{q=0}^{Q} y_{pq} \phi_p^P(\xi) \phi_q^Q(\eta) \qquad (4.5)$$

For a subdomain, the boundaries of which include a rough surface, numerical tests have been performed. Based on results of the numerical tests, we observed that upon a proper identification of the *local* maxima and minima of *x* and *y*, the linear transformation can yield the same coordinate mapping as that obtained by the curvilinear transformation. Hence, we may use the linear transformation with properly identified local maxima and minima of *x* and *y* for coordinate mapping of a subdomain, the boundaries of which include a rough surface.

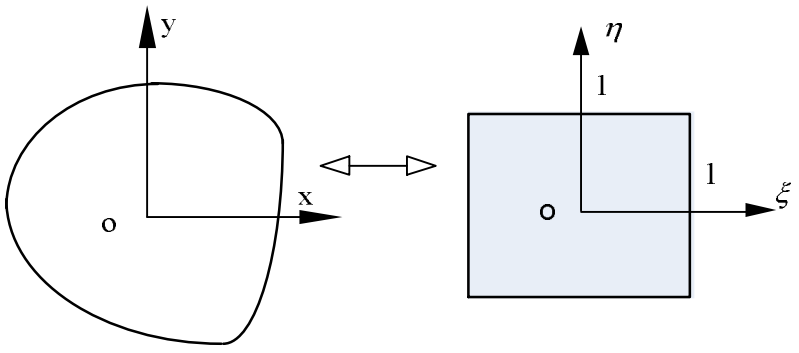

Fig. 4.3 Subdomain mapping from a curved quadrilateral to a unit square.

Then, making use of the coordinate transformation $\xi = \xi(x, y), \quad \eta = \eta(x, y),$ the 2-D Maxwell's equations for TM_z polarization in the (x, y) coordinates,

$$\begin{aligned}
\frac{\partial H_x}{\partial t} &= -\frac{1}{\mu}\frac{\partial E_z}{\partial y}, \\
\frac{\partial H_y}{\partial t} &= \frac{1}{\mu}\frac{\partial E_z}{\partial x}, \\
\frac{\partial E_z}{\partial t} &= \frac{1}{\varepsilon}\left(\frac{\partial H_y}{\partial x} - \frac{\partial H_x}{\partial y}\right) - \frac{\sigma}{\varepsilon}E_z,
\end{aligned} \tag{4.6}$$

can be rewritten in the (ξ, η) coordinate system in matrix form as

$$\frac{\partial q}{\partial t} + A\frac{\partial q}{\partial \xi} + B\frac{\partial q}{\partial \eta} + Cq = 0, \tag{4.7}$$

where $q = (H_x, \ H_y, \ E_z)^T$, A, B, and C are the coefficient matrix,

$$A = \begin{pmatrix} 0 & 0 & \frac{\xi_y}{\mu} \\ 0 & 0 & \frac{-\xi_x}{\mu} \\ \frac{\xi_y}{\varepsilon} & \frac{-\xi_x}{\varepsilon} & 0 \end{pmatrix}, \quad B = \begin{pmatrix} 0 & 0 & \frac{\eta_y}{\mu} \\ 0 & 0 & \frac{-\eta_x}{\mu} \\ \frac{\eta_y}{\varepsilon} & \frac{-\eta_x}{\varepsilon} & 0 \end{pmatrix}, \quad C = \begin{pmatrix} 0 & 0 & 0 \\ 0 & 0 & 0 \\ 0 & 0 & \frac{\sigma}{\varepsilon} \end{pmatrix}, \tag{4.8}$$

$\xi_x = \partial\xi / \partial x, \quad \xi_y = \partial\xi / \partial y$ etc.

4.2.3 Chebyshev Spectral Collocation Procedure

After the coordinate mapping, the Chebyshev spectral collocation procedure [26-32] is performed for treating the electromagnetic field quantities and their spatial derivatives in the transformed (ξ, η) coordinates. First, the grid points in the transformed coordinates are chosen as the tensor-product Chebyshev-Gauss-Lagrange (CGL) points,

$$\begin{aligned} \xi_i &= -\cos\left(\frac{i\pi}{N}\right), \quad i = 0,1,...N \\ \eta_j &= -\cos\left(\frac{j\pi}{M}\right), \quad j = 0,1,...M. \end{aligned} \tag{4.9}$$

Then, the electromagnetic field quantities are represented by a tensor-product Chebyshev-Lagarange polynomial

$$q(\xi,\eta) = \sum_{i=0}^{N}\sum_{j=0}^{M} q\left(\xi_i,\eta_j\right) g_i(\xi) g_j(\eta), \tag{4.10}$$

where the Lagrange interpolation polynomials are defined by

$$\mathrm{g}_i\left(\alpha\right) = \frac{\left(1-\alpha^2\right)T'_N\left(\alpha\right)(-1)^{i+N+1}}{c_i N^2\left(\alpha-\alpha_i\right)}\ , \tag{4.11}$$

in which $\alpha = (\xi,\eta)$, $c_i = 1+\delta_{i0}+\delta_{iN}$, and $T_N(x)$ is the N^{th}-order Chebyshev polynomial $T_N(x) = \cos(N\cos^{-1}x)$.

Finally, the spatial derivatives of the field quantities at the grid points are obtained in terms of the derivatives of the Lagrange polynomials as

$$\frac{\partial q(\xi_i,\eta_j)}{\partial \xi} = \sum_{k=0}^{N} D_{ik}^{\xi} q\left(\xi_k,\eta_j\right),$$
$$\frac{\partial q(\xi_i,\eta_j)}{\partial \eta} = \sum_{k=0}^{M} D_{jk}^{\eta} q\left(\xi_i,\eta_k\right), \tag{4.12}$$

where the differentiation matrix D_{ik}^{α} is given by

$$\mathrm{D}_{ik}^{\alpha} = \begin{cases} -\dfrac{c_i}{c_k}\dfrac{(-1)^{i+k}}{\alpha_k-\alpha_i} & i \neq k, \\ -\dfrac{\alpha_k}{2\left(1-\alpha_k^2\right)} & 1 \le i = k \le N\text{-}1, \\ -\dfrac{2N^2+1}{6} & i = k = 0, \\ \dfrac{2N^2+1}{6} & i = k = N. \end{cases} \tag{4.13}$$

4.2.4 Implementation of Well-Posed PML

In order to truncate the unbounded medium and confine the solution in a finite computational domain, an absorbing boundary condition (ABC) is introduced. The ABC is introduced by implementing a well-posed perfectly matched layer (PML) [33-39] surrounding the "regular" region. In the PML region, the complex coordinate-stretching variables

$$\partial x \Rightarrow \left[1+\frac{i\omega_x(x)}{\omega}\right]\partial x, \quad \partial y \Rightarrow \left[1+\frac{i\omega_y(y)}{\omega}\right]\partial y, \tag{4.14}$$

are applied to rewrite the Maxwell's equations for the electromagnetic field in the PML region. Defining new field variables for the PML region,

$$\hat{H}_x = H_x + \omega_x Q_x, \quad \hat{H}_y = H_y + \omega_y Q_y, \tag{4.15}$$

the Maxwell's equation in the PML region can be written as

$$\begin{aligned}
&\frac{\partial \hat{H}_x}{\partial t} = -\frac{1}{\mu}\frac{\partial E_z}{\partial y} + \left(\omega_x - \omega_y\right)(\hat{H}_x - \omega_x Q_x), \\
&\frac{\partial \hat{H}_y}{\partial t} = \frac{1}{\mu}\frac{\partial E_z}{\partial x} + \left(\omega_y - \omega_x\right)(\hat{H}_y - \omega_y Q_y), \\
&\frac{\partial E_z}{\partial t} = \frac{1}{\varepsilon}\left(\frac{\partial \hat{H}_y}{\partial x} - \frac{\partial \hat{H}_x}{\partial y}\right) - \frac{\sigma}{\varepsilon}E_z - \left(\omega_x + \omega_y\right)E_z, \\
&-\left[\frac{\sigma}{\varepsilon}\left(\omega_x + \omega_y\right) + \omega_x\omega_y\right]P_z - \frac{\sigma}{\varepsilon}\omega_x\omega_y K_z,
\end{aligned} \tag{4.16}$$

where

$$\frac{\partial Q_x}{\partial t} = \hat{H}_x - \omega_x Q_x, \tag{4.17}$$

$$\frac{\partial Q_y}{\partial t} = \hat{H}_y - \omega_y Q_y, \tag{4.18}$$

$$\frac{\partial P_z}{\partial t} = E_z, \tag{4.19}$$

$$\frac{\partial K_z}{\partial t} = P_z. \tag{4.20}$$

Appropriate profiles of ω_x and ω_y are selected for the complex coordinate-stretching variables, which will result in the desired absorbing boundary condition.

4.2.5 Subdomain Patching

In the multidomain PSTD algorithm, after the solution in each individual subdomain, the fields at the interfaces between adjacent subdomains do not naturally satisfy the boundary conditions. And we need to pass information between the subdomains to recover the global solutions. This is done by means of the subdomain patching, [26, 27], that is, at an interface separating two subdomains, we enforce the physical boundary conditions that require continuity of the tangential components of the electric and magnetic field at a dielectric interface; and zero tangential electric field component and normal magnetic field component on a perfect electric conductor (PEC) surface.

4.2.6 Plane Wave Excitation and TF/SF Formulation

In the past, the total field/scattered field (TF/SF) formulation [26, 40, 41] and the pure scattered field method [42, 43] have both been employed to implement a plane wave incidence in the PSTD algorithm for the solution of scattering problems. However, as pointed out in [27], the pure scattered field method is potentially complicated if a complex surface shape is involved. Since our goal is to solve the scattering problem of an object buried below a random rough surface, which is of complex surface shape, the scattered field method is not a good choice. Therefore, we select employing the TF/SF formulation to enforce the plane wave excitation. The total field is calculated in the interior region and the scattered field is computed in exterior region. Then, the boundary

condition requirements of continuity of the tangential components of the electric and magnetic field are enforced at the interfaces between these two regions.

4.2.7 Time Stepping

The 2-D Maxwell's equations formulated in the (ξ, η) coordinates contain both spatial derivatives and time derivatives. The *spatial derivatives* of the field quantities at the grid points are obtained in terms of the derivatives of the Lagrange polynomials, in the Chebyshev spectral collocation procedure presented in Section 4.2.3. To take care of the *time derivatives*, we use a fourth order, five-stage Runge-Kutta method [26, 27, 44-46] for the time integration to advance the solution to the next time step as

$$\frac{\partial \mathrm{q}}{\partial t} = f\left(t, \mathrm{q}\right), \tag{4.21}$$

where

$$f = -(A\frac{\partial \mathrm{q}}{\partial \xi} + B\frac{\partial \mathrm{q}}{\partial \eta} + C\mathrm{q}), \tag{4.22}$$

and denoting $q(t_{n+1})$ as q_{n+1} where $t_n = n\Delta t$ and Δt is the time step size. The Runge-Kutta method procedure is described as

$$\begin{aligned} &q_0 = q_n, \\ &\forall j \in [1,5]: \begin{cases} k_j = a_j k_{j-1} + \Delta t f\left(\left(n + c_j\right)\Delta t, q_{j-1}\right) \\ q_j = q_{j-1} + b_j k_j \end{cases}, \\ &q_{n+1} = q_5. \end{aligned} \tag{4.23}$$

In equation (4.23), Δt is the time step length and is determined from the stability criterion,

$$\frac{c\Delta t}{\Delta x} \le \frac{2}{\sqrt{D\pi}}, \tag{4.24}$$

where D is the dimensionality of the problem.

4.3. Numerical Results of the Scattering of a Cylinder in Open Space

The multidomain PSTD algorithm formulated in the previous section is implemented into computer programming. The program flow chart is shown in Fig. 4.4.

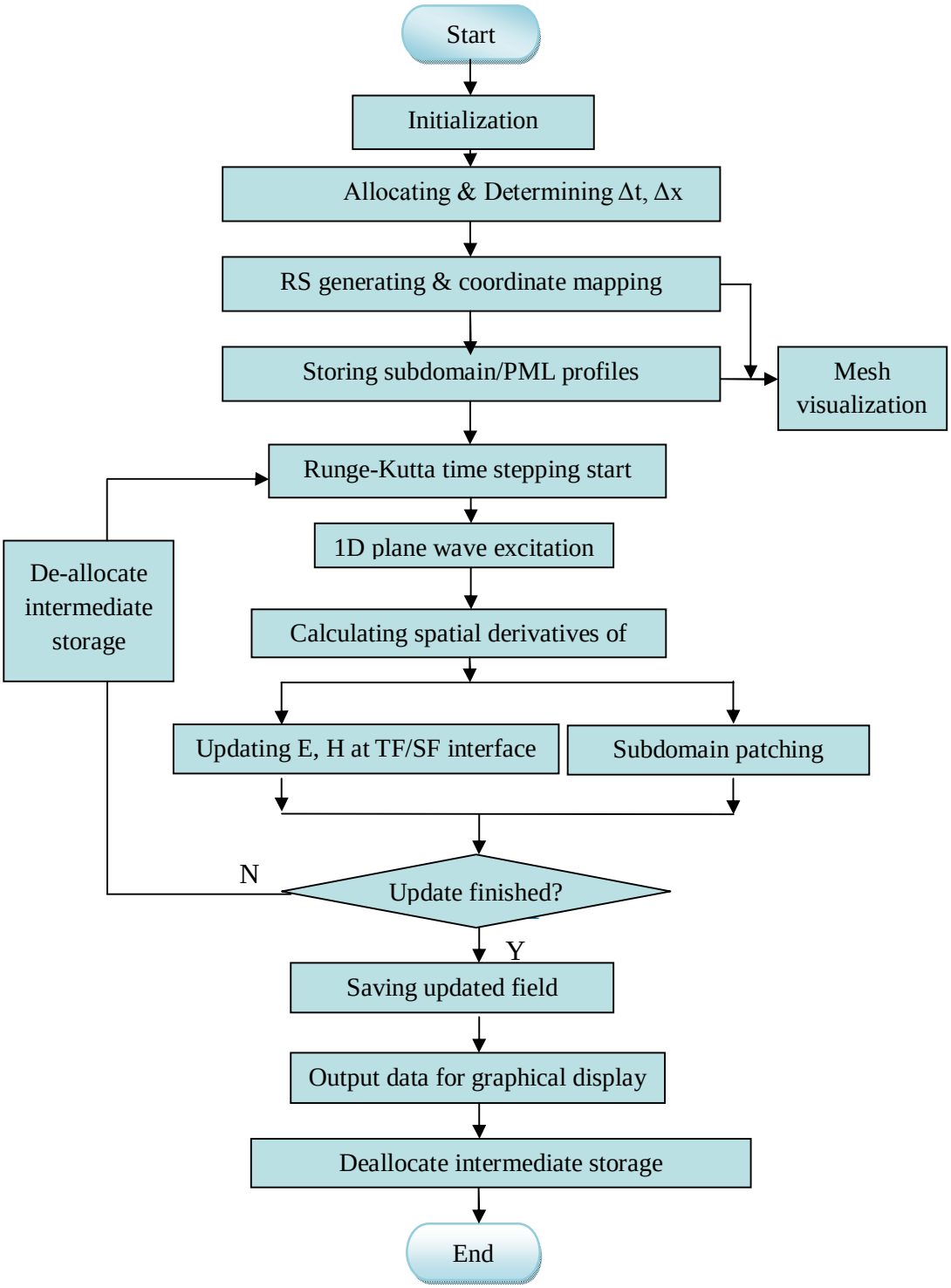

Fig. 4.4 Program flowchart of Multidomain PSTD algorithm.

Using the multidomain PSTD algorithm and the computer codes, sample numerical results are obtained and shown in this section. For the numerical results presented, the time-domain function of the incident plan wave is taken to be the first derivative of Blackman-Harris window function,

$$W_{bhw1^{st}}(t)=\begin{cases}-\sum_{n=1}^{3}\frac{n\pi}{T}a_n\sin\left(\frac{2n\pi t}{T}\right), & 0<t<T\\ 0, & otherwise\end{cases}, \tag{4.25}$$

where a_1=-0.488, a_2=0.145, a_3=-0.01022222 and T=1.55/*f*, *f* is the central frequency, which is taken to be 50MHz for the numerical results presented in this section.

First, we consider the plane wave propagation in an open space – no scatterer is there, the geometry of which is shown in Fig. 4.5(a). The multidomain PSTD algorithm is employed to calculate the total electric field at a point (*-2.1036, 2.1036*), its plot is compared with that of the incident filed there. From the comparison depicted in Fig. 4.5(b), one observes that the two curves fall on top of each other as expected.

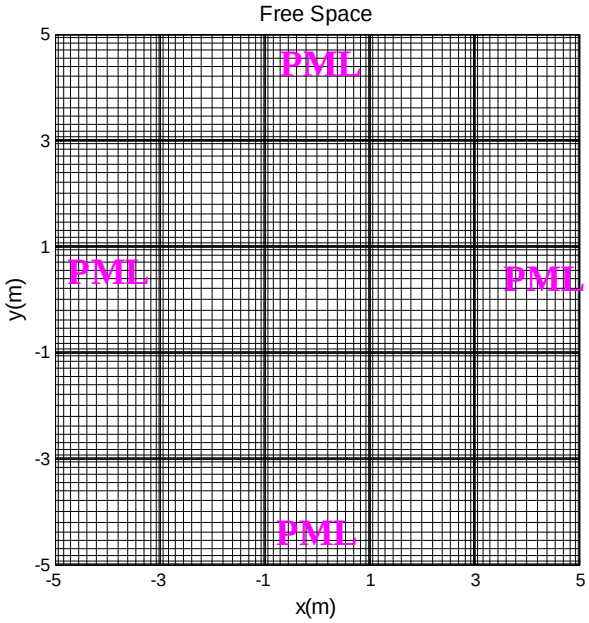

(a)

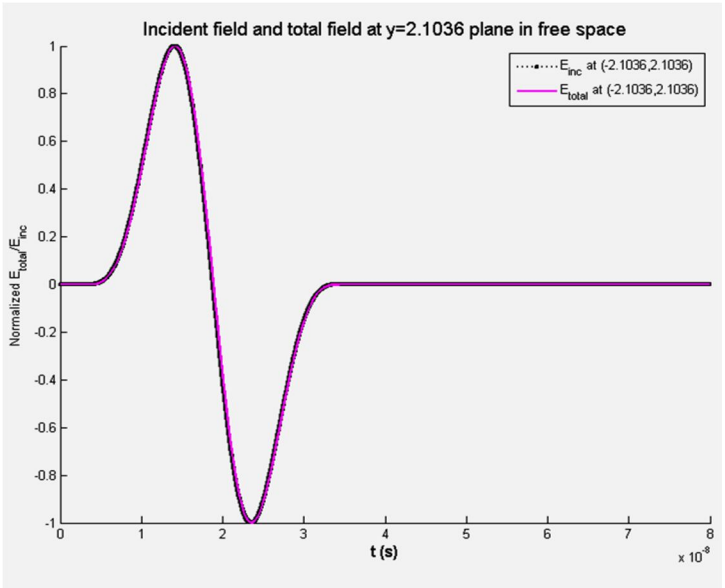

(b)

Fig. 4.5 Plane wave propagation in free space (a) Computation domain, (b) Comparison of E_{inc} and E_{total}.

Second, we compare the tangential component of the magnetic field at the center point on the illuminated side of a rectangular PEC cylinder with that of the incident magnetic field, under a plane wave normal incidence. The geometry and the numerical result are presented in Figs. 4.6(a) and 4.6(b). As shown in Fig. 4.6(b), the magnitude of the tangential component of the total magnetic field observed at the center of the illuminated side of the regular PEC cylinder is about equal to that of the incident field doubled, as one would expect.

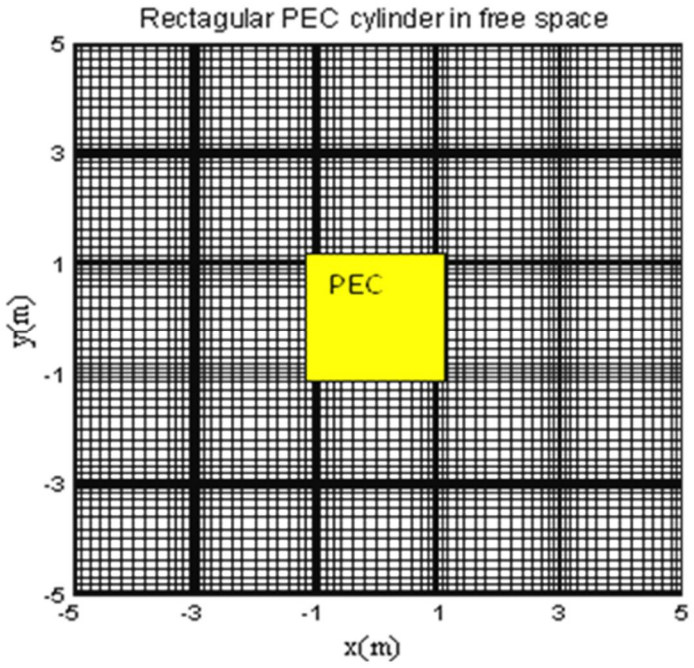

(a)

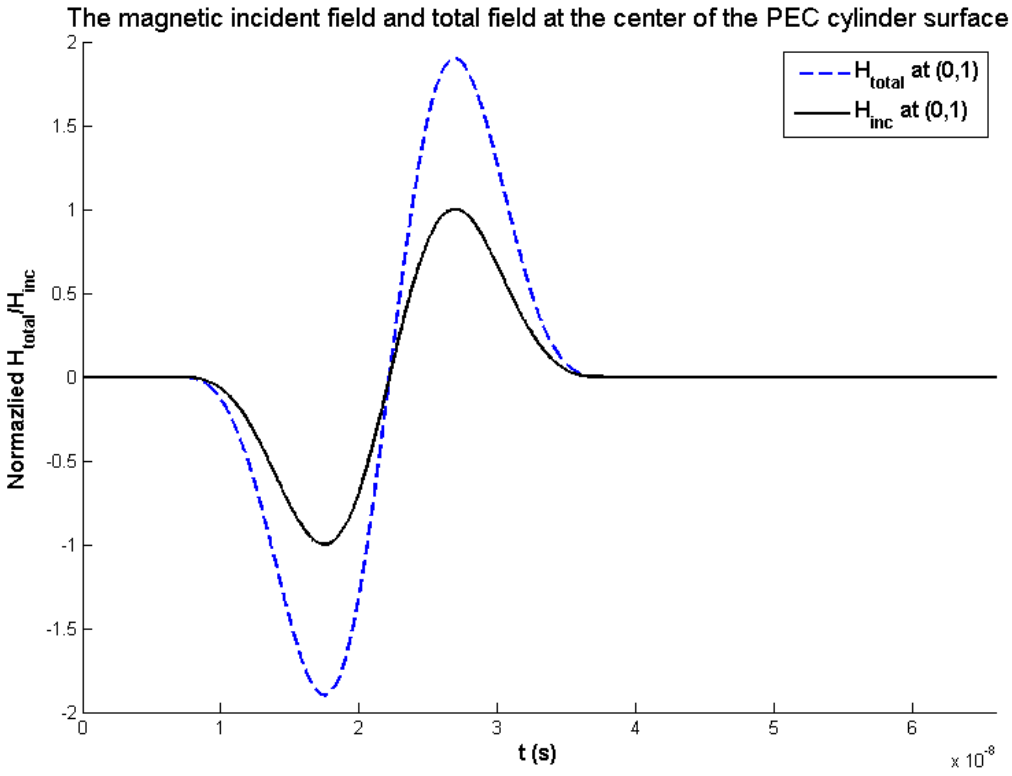

(b)

Fig. 4.6 The computed tangential components of the magnetic fields

(a) Geometry, (b) Comparison of H_{total} and H_{inc} at the center of the illuminated surface of the rectangular PEC cylinder.

The third sample numerical result is for the scattering of a circular PEC cylinder under a plane wave normal incidence. The geometry of the computation domain is depicted in Fig. 4.7(a). The numerical result is compared with the analytical solution, which is obtained by transferring the frequency domain solution [47]

$$E_z = E_0^i e^{-jk\rho\cos\phi} - E_0^i \sum_{n=-\infty}^{\infty} j^{-n} \frac{J_n(ka)}{H_n^{(2)}(ka)} H_n^{(2)}(k\rho) e^{jn\phi}. \tag{4.26}$$

to time-domain. Fourier transformation and inverse Fourier transformation are applied.

The comparison between these two sets of data illustrated in Fig. 4.7(b) shows an excellent agreement.

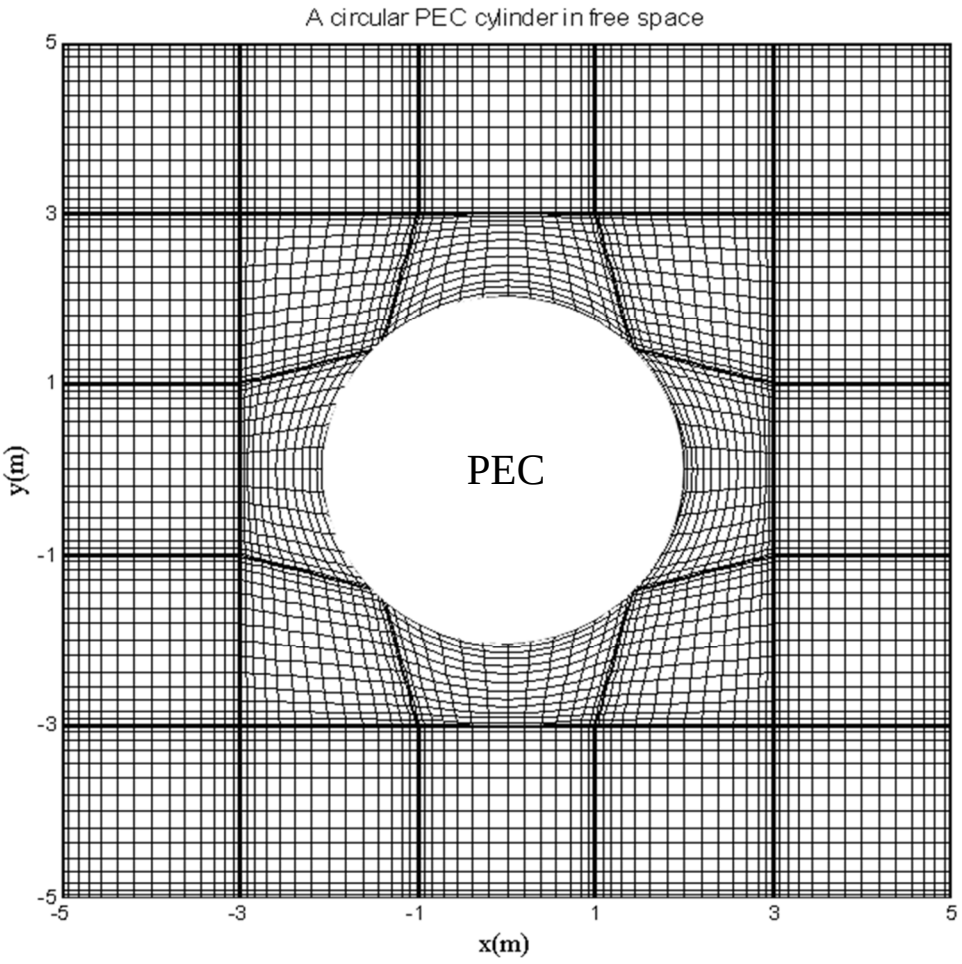

(a)

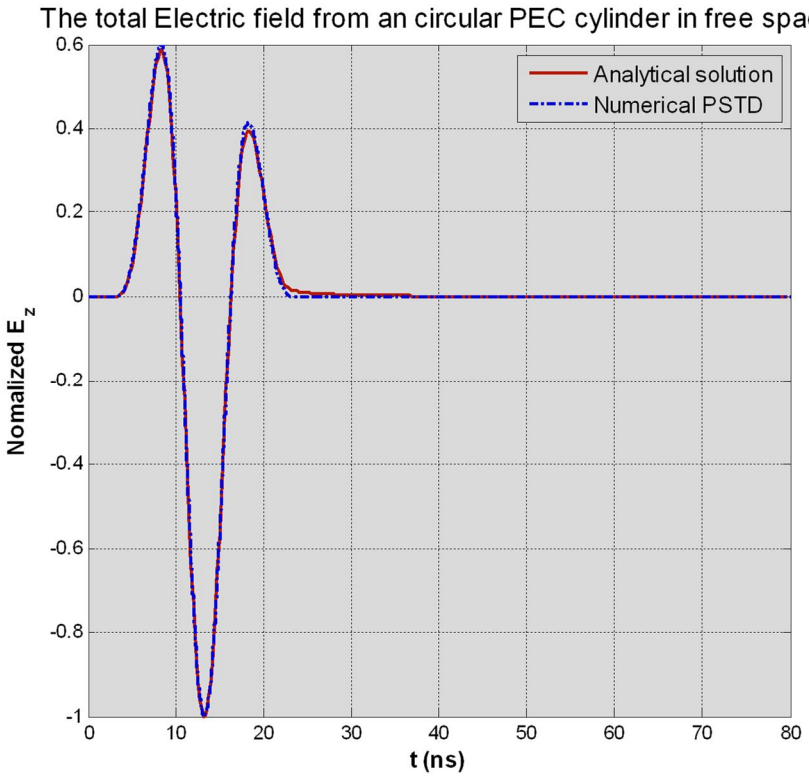

(b)

Fig. 4.7 Plane wave scattering from a circular PEC cylinder in free space

(a) Geometry, (b) Comparison of the PSTD numerical result with analytical solution.

4.4 Formulation of the Numerical Method for Determining Electromagnetic Scattering of Buried Cylinder below a Random Rough Surface

The multidomain PSTD algorithm presented above is further developed and then combined with the Monte-Carlo method in this section, for studying the scattering of a 2-D object buried below a random rough surface. In the development, special attention is paid to the random rough surface separating two semi-infinite homogeneous spaces, and a few important issues are addressed blow.

4.4.1 Generation of Random Rough Surface Profile and Its Matching with CGL Points

A random rough surface with Gaussian spectrum profile $y = f(x)$ [48] can be generated as the follows. First, a set of uniformly distributed sampling points is selected by

$$x_m = mL / N, \tag{4.27}$$

where L is the length of the random rough surface, N is the number of the sample points. Then the rough surface profile can be obtained using the inverse Fourier transform

$$y = f(x_m) = \frac{1}{L} \sum_{n=-\frac{N}{2}+1}^{\frac{N}{2}} b_n \exp\left(i \frac{2\pi nm}{N} \right), \tag{4.28}$$

where the inverse Fourier transform coefficients are given by

$$b_n = \begin{cases} \sqrt{2\pi LW(0)r_\alpha}, n = 0; \\ \sqrt{2\pi LW(\frac{\pi N}{L})r_\beta}, n = \frac{N}{2}; \\ \sqrt{2\pi LW(|k_n|)}[\frac{1}{\sqrt{2}}(r_\sigma + ir_\zeta)], n = -\frac{N}{2}+1, ..., -2, -1; \\ \{\sqrt{2\pi LW(|k_{-n}|)}[\frac{1}{\sqrt{2}}(r_\sigma + ir_\zeta)]\}^*, n = 1, 2, ..., \frac{N}{2}-1; \end{cases} \tag{4.29}$$

in which r_σ and r_ξ are random numbers and

$$W(k_n) = \frac{h^2 l}{2\sqrt{\pi}} e^{-(\frac{\pi n}{L} l)^2}, \tag{4.30}$$

where *h* and *l* are the *rms* height and the correlation length of the random rough surface. The roughness of generated surface can be adjusted by changing the combined values of *h* and *l*. The derivative of the rough surface profile can be approximated by means of finite difference as

$$f'(x_m) = \frac{f(x_{m+1}) - f(x_{m-1})}{2\Delta x}. \tag{4.31}$$

A sample random rough surface with Gaussian spectrum profile is depicted in Fig. 4.8 in blue color. Note that the random rough surface profile $y = f(x_m)$ is generated as a function of x_m. But in a PSTD subdomain that is partially bounded by the rough surface, the profile y_{mapped} is a function of x_{mapped}. Both x_{mapped} and y_{mapped} are related to the CGL points in the (ξ, η) coordinate by the coordinate transformation. Since x_m are uniformly distributed but x_{mapped} are not, they are normally different; hence the two profiles of y =

$f(x_m)$ and y_{mapped} in general do not coincide. However, for each point x_{mapped}, there is a point x_m adjacent to it; and since the profile of the rough surface is a one-dimensional function, a polynomial can be found to interpolate between the two set of data [$x_{profile}$, $y_{profile}$] and [x_{mapped}, y_{mapped}], and a Cubic Spline Interpolation polynomial is used for the interpolation. A comparison of the random rough surface profile with Gaussian spectrum and that obtained using the mapped CGL points is presented in Fig. 4.8, from which we observe that these two profiles almost fall on top of each other. Then, using the values of $y = f(x_m)$ (or equivalently y_{mapped}) on the random rough surface profile, the other grid points within a subdomain that is partially bounded by the random rough surface can be determined.

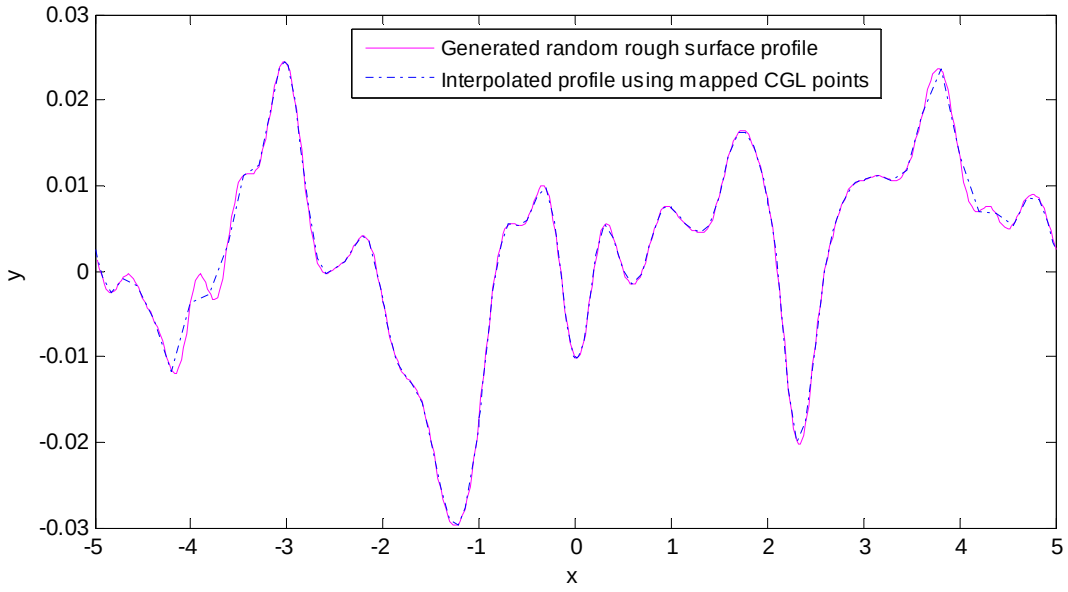

Fig. 4.8 Comparison of the random rough surface profile with Gaussian spectrum and that obtained using the mapped CGL points.

4.4.2 Determination of the Time-Domain Composite Fields in a Two-Half-Space Region and Its Implementation in the TF/SF Formulation

The incident wave driving the scattering of a buried object is different from that of an object in an open space. It should be determined by a "Three-wave approach", which was used in FDTD analysis for the scattering of an object buried below planar interfaces [49] – [51]. The driving composite field determined from the "Three-wave approach", is extended for the analysis of the scattering of a cylinder buried below a random rough surface. As shown in Fig. 4.9, a virtual planar interface is placed at $y=0$ along the rough surface for the calculation of the driving composite field. The random rough surface just causes additional inhomogeneties above/below the virtual planar interface; and these inhomogeneities can be treated as "additional scatterers" touching the virtual surface, illuminated by the composite fields.

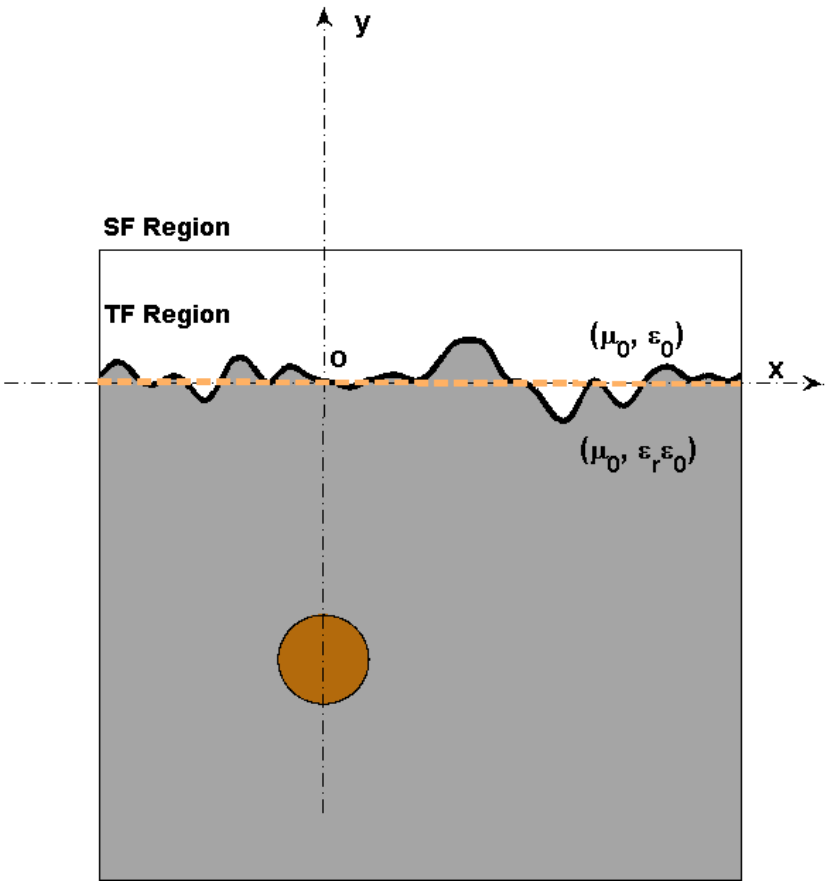

Fig. 4.9 A cylinder buried below a random rough surface and a virtual planar interface placed along the rough surface.

As pointed out in [49], the driving incident wave impinging on an object near the media interface is the composite of the initial incident, reflected, and transmitted waves. In the upper half space, the driving composite field is the sum of the initial incident field plus the reflected field

$$\vec{E}_{inc} = \vec{E}_{initial,inc} + \vec{E}_{ref},$$
$$\vec{H}_{inc} = \vec{H}_{initial,inc} + \vec{H}_{ref}; \tag{4.32}$$

and in the lower half space, the driving composite field (the driving incident field to the buried cylinder) is the transmitted field

$$\vec{E}_{inc} = \vec{E}_{trans},$$
$$\vec{H}_{inc} = \vec{H}_{trans}. \tag{4.33}$$

The initial incident field, the reflected and the transmitted field can be calculated analytically in absence of the scatterer in time domain, taking into account the time delay for the fields to reach a point on the TF/SF interface separating the TF and SF regions. Such calculated driving composite fields can be readily enforced on the TF/SF interface in the multidomain PSTD algorithm. Assume that a TM_z initial plane wave impinges at (x_0, y_0) located by $\vec{r}_0$, as shown in Fig. 4.10. In the upper half space, at an arbitrary point (x, y) on the TF/SF interface, the initial incident field is

$$f(t - \frac{\hat{k}_i \bullet \vec{r}}{c}) = f[t - \left(\frac{-x\sin\theta_i - y\cos\theta_i}{c} \right)], \tag{4.34}$$

where $\hat{k}_i = -\sin\theta_i \hat{x} - \cos\theta_i \hat{y}$, in which θ_i is the incident angle. For the reflected field, from *(x, y)* draw a line parallel to $\hat{k}_r$ and intersecting the x axis at $(x_r^{'}, y_r^{'})$ as illustrated in Fig. 4.10, where $\hat{k}_r = -\sin\theta_i \hat{x} + \cos\theta_i \hat{y}$, $x_r^{'} = x + y\tan\theta_i$, and $y_r^{'} = 0$. The time needed for the reflected wave to travel from $(x_r^{'}, y_r^{'})$ to *(x, y)* is $t_r = \frac{d_r}{c} = \frac{y\cos\theta_i - \left(x - x_r^{'}\right)\sin\theta_i}{c}$.

From eq. (4.33), the travel time for the initial incident wave to reach $(x_r^{'}, y_r^{'})$ can be calculated by $t_{inc}^{'} = \frac{-x_r^{'} \sin\theta_i}{c}$. Thus, in the upper half space, the composite incident field, as the sum of the initial incident field and the reflected field, to be enforced on the TF/SF interface can be obtained by

$$f[t - \left(\frac{-x\sin\theta_i - y\cos\theta_i}{c}\right)] + \Gamma_e f\left(t - t_{inc}^{'} - t_r\right), \tag{4.35}$$

where the reflection coefficient, $\Gamma_e = \frac{\eta_b \cos\theta_i - \eta_0 \cos\theta_t}{\eta_b \cos\theta_i + \eta_0 \cos\theta_t}$, η_0 and η_b are the characteristic impedance of the upper and lower half space respectively.

Finally, the composite incident electric field can be computed by

$$E_z^i = E_0^i f\left[t - \left(\frac{-x\sin\theta_i - y\cos\theta_i}{c}\right)\right] + \Gamma_e E_0^i f\left(t - t_{inc}^{'} - t_r\right). \tag{4.36}$$

To get the composite incident magnetic field H_{inc}, we apply $\vec{H} = \frac{1}{\eta_0}\left(\hat{k} \times E_z \hat{z}\right)$ and then obtain

$$\begin{aligned} H_x^i &= -\frac{E_0^i}{\eta_0}\cos\theta_i f\left[t - \left(\frac{-x\sin\theta_i - y\cos\theta_i}{c}\right)\right] + \Gamma_e \frac{E_0^i}{\eta_0}\cos\theta_i f\left(t - t_{inc}^{'} - t_r\right), \\ H_y^i &= \frac{E_0^i}{\eta_0}\sin\theta_i f\left[t - \left(\frac{-x\sin\theta_i - y\cos\theta_i}{c}\right)\right] + \Gamma_e \frac{E_0^i}{\eta_0}\sin\theta_i f\left(t - t_{inc}^{'} - t_r\right). \end{aligned} \tag{4.37}$$

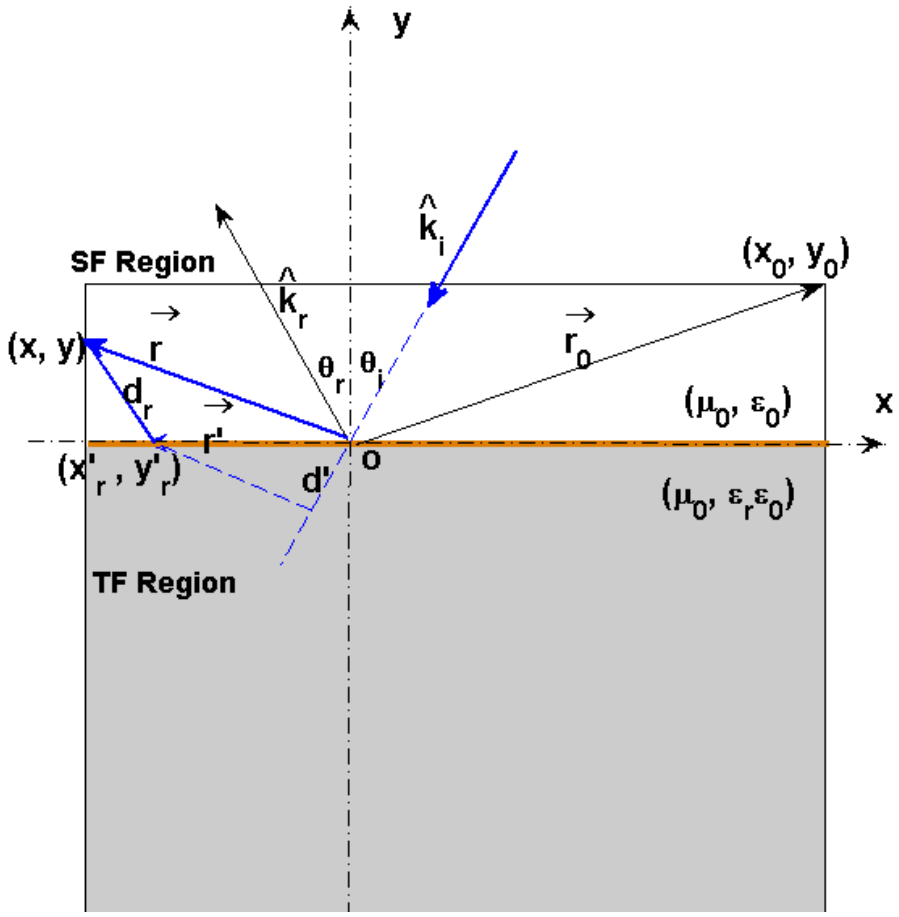

Fig. 4.10 Geometry for the calculation of the composite field in the upper half space.

Similarly, in the lower half space, the composite incident field to the buried cylinder, which is the transmitted field, to be enforced on the TF/SF interface can be determined by

$$E_z^i = \tau_e E_0^i f\left(t - t_{inc}^{"} - t_{trans}\right),$$
$$H_x^i = -\frac{\sqrt{\varepsilon_r}}{\eta_0}\tau_e E_0^i \cos\theta_t f\left(t - t_{inc}^{"} - t_{trans}\right), \tag{4.38}$$
$$H_y^i = \frac{\sqrt{\varepsilon_r}}{\eta_0} E_0^i \tau_e \sin\theta_t f\left(t - t_{inc}^{"} - t_{trans}\right),$$

where the transmission coefficient $\tau_e = \dfrac{2\eta_b \cos\theta_t}{\eta_0 \cos\theta_i + \mu\eta_b \cos\theta_t}$, $t"_{inc}$ and t_{trans} can be determined from the geometry shown in Fig. 4. 11.

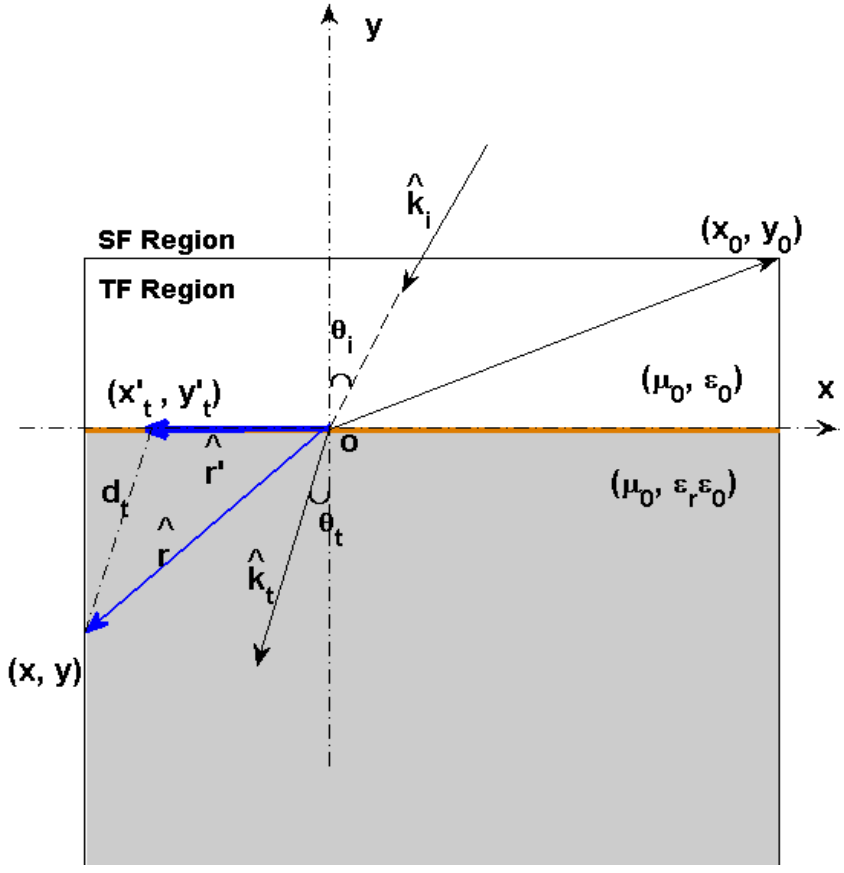

Fig. 4.11 Geometry for the calculation of the composite field in the lower half space.

A similar procedure can be developed for determining the TE_z composite incident wave.

4.4.3 Subdomain Patching for Subdomains Separated by a Random Rough Surface

As presented in Section 4.2.5, in the multidomain PSTD algorithm, after the solution in each individual subdomain, the subdomain patching is necessary and is executed by enforcing the physical boundary conditions. For this purpose, we need to decompose each field component into the tangential and normal component on the subdomain interface. Obviously, for the analysis of an object buried below a random rough surface, part of a subdomain interface could be a rough surface. As shown in Fig. 4.12, at a grid point on the random rough surface, the unit vector normal to the surface can be found by

$$\hat{n} = \frac{-f'(x)\hat{x} + \hat{y}}{\sqrt{1 + f'(x)^2}}, \tag{4.39}$$

and the unit vector tangential to the surface is

$$\hat{t} = \frac{\hat{x} + f'(x)\hat{y}}{\sqrt{1 + f'(x)^2}}. \tag{4.40}$$

In equations (4.39) and (4.40), *f'(x)* is the slope of the random rough surface at that point and can be found from equation (4.31) in section 4.4.1. Using these two equations, we

can extract the normal and tangential component of the fields by taking dot products of $\hat{n}$ or $\hat{t}$ with the corresponding fields.

$$
\begin{aligned}
E_z &= E_z, \\
H_{1t} &= \hat{t} \bullet (H_{1x}\hat{x} + H_{1y}\hat{y}), \\
H_{1n} &= \hat{n} \bullet (H_{1x}\hat{x} + H_{1y}\hat{y}).
\end{aligned}
\qquad (4.41)
$$

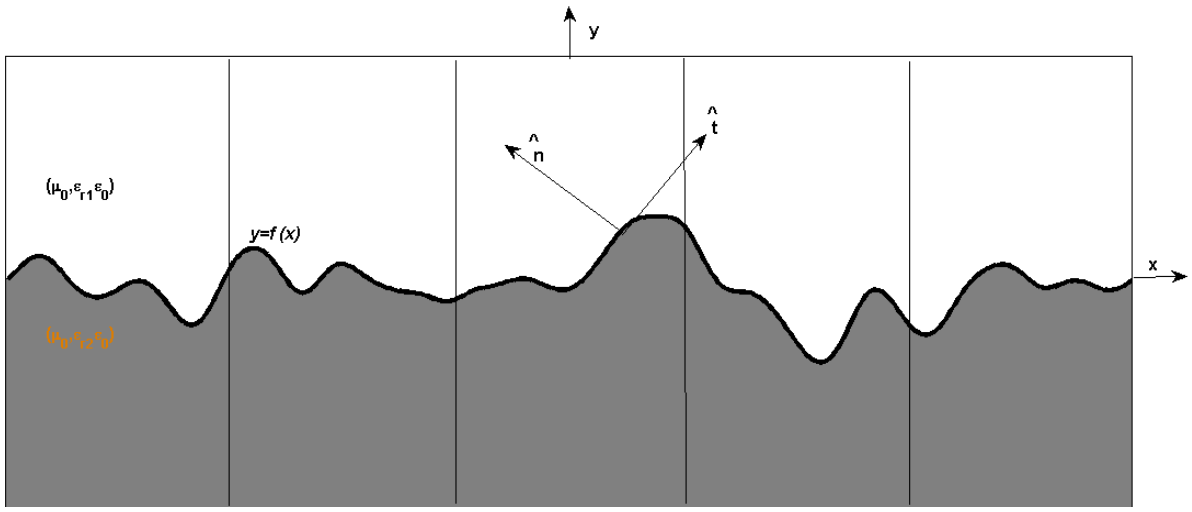

Fig. 4.12 The tangential and normal unit vector on a random rough surface.

Then, by enforcing the boundary condition that the tangential components of the fields must be continuous and the normal components of the fields are left unchanged on a random rough surface separating two dielectric media, we have

$$H_{1t}^{'} = H_{2t}^{'} = H_{t}^{'} = \frac{1}{2}\left(H_{1t} + H_{2t}\right),$$
and
$$H_{1n}^{'} = H_{1n} \text{ and } H_{2n}^{'} = H_{2n}. \tag{4.42}$$

Combining equations (4.39)--(4.42), the updated electric field for TM_z polarization can be determined by

$$E'_{z_{\frac{1}{2}}} = \frac{1}{2}(E_{z1} + E_{z2}), \tag{4.43}$$

and the updated magnetic field components are found to be

$$H_{1x}' = \frac{1}{2}\frac{1}{1+f'(x)^2}[H_{1x} + H_{2x} + f'(x)(H_{1y} + H_{2y})] - \frac{f'(x)}{1+f'(x)^2}[-f'(x)H_{1x} + H_{1y}], \tag{4.44}$$

$$H_{1y}' = \frac{1}{2}\frac{f'(x)}{1+f'(x)^2}[H_{1x} + H_{2x} + f'(x)(H_{1y} + H_{2y})] + \frac{1}{1+f'(x)^2}[-f'(x)H_{1x} + H_{1y}], \tag{4.45}$$

in region 1 and

$$H_{2x}' = \frac{1}{2}\frac{1}{1+f'(x)^2}[H_{1x} + H_{2x} + f'(x)(H_{1y} + H_{2y})] - \frac{f'(x)}{1+f'(x)^2}[-f'(x)H_{2x} + H_{2y}], \tag{4.46}$$

$$H_{2y}' = \frac{1}{2}\frac{f'(x)}{1+f'(x)^2}[H_{1x} + H_{2x} + f'(x)(H_{1y} + H_{2y})] + \frac{1}{1+f'(x)^2}[-f'(x)H_{2x} + H_{2y}], \tag{4.47}$$

in region 2.

4.4.4 Monte-Carlo Statistic Average

Due to the random nature of the rough surface involved in this research, a statistic average of the scattering of buried object needs to be determined. As pointed in [52], the Monte-Carlo method (MCM) is also known as the method of statistical trials. It is a method of approximately solving problems using sequences of random numbers. This method has been used in the past together with an integral equation formulation in the frequency domain [53, 54] and with FDTD method in the time domain [55, 56] for the analysis of electromagnetic scattering involving a random rough surface. In this work, the Monte-Carlo analysis is carried out by the following steps. First, a set of random rough surfaces with Gaussian spectrum is generated. Then, the multidomain PSTD algorithm formulated in the previous sections is employed to determine the scattering of a buried object below each of the rough surfaces generated. And finally, the statistic average of the scattering is determined after a series of numerical tests to make sure that it converges.

CHAPTER 5

CONCLUSIONS

Studies on two subjects are presented in this dissertation. In Chapter 2, a computer simulation is presented for tracking the smallest distance between the overhead power line conductors in transition spans that are often required in practical power line structures. Information of the smallest distance between the power line conductors is useful for predicting the probability of the magnetically induced subsequent fault. The simulation is based on coordinate transformations and a dynamic analysis. Sample numerical results are presented, analyzed, and validated. From the numerical results presented, we observe that the construction/structural geometry of the transition spans as well as their sags may significantly affect the probability of the subsequent fault.

The numerical technique developed has been implemented into the upgrade of software for the analysis of magnetic induced subsequent fault (MISFault) in utility line topologies. As shown in Chapter 3, the software is capable of predicting the smallest distance between the power line conductors during their swing procedure, from which one can predict the probability of the magnetically induced subsequent fault; and determine the allowed span length range from consideration of eliminating the subsequent fault, which is anticipated to be useful for a utility in long span design. It has been tested and the accuracy of its computation results has been validated by checking with the energy conservation law requirement. The MISFault software is being used by

Duke Energy Company and is expected to be useful to a utility for eliminating the magnetically induced subsequent fault.

A multidomain pseudospectal time domain (PSTD) algorithm is developed and presented in Chapter 4 for the analysis of scattering of a 2-D cylinder located in free space. The algorithm has been validated by comparing its numerical result with the analytical solution. After the validation, the theoretical derivations are extended for the analysis of objects buried below a random rough surface and a few important issues have been addressed. In the future work, the analysis will be carried out for the analysis of a 2-D cylinder, then a 3-D object buried below a random rough surface, and finally a 3-D object buried in a layered structure with a random rough surface.

APPENDIX

COMPUTATION OF THE MAGNETIC FLUX DENSITY

The magnetic flux density $\vec{B}_i$ observed at a point on phase *i* (*i* = *a, b, c*) conductor is produced by the current I_i in itself and the currents I_j ($j = a, b, c, \quad j \neq i$) in the other two phase conductors, and

$$\vec{B}_i = \vec{B}_{ii} + \sum_j \vec{B}_{ij,i}, \tag{A1}$$

where $\vec{B}_{ii}$ is due to its own current and can be calculated in the (X_i, Y_i, Z_i) coordinate system as presented in [2]. But $\vec{B}_{ij,i}$ counts the contributions from the other two phase currents and it must be computed in a different way as described in the following two major steps. First, we use Biot-Savart's law to compute the magnetic flux density,

$$\vec{B}_{ij,j} = \frac{\mu_0 I_j}{4\pi} \int \frac{d\vec{l}_j \times \vec{R}_{ij}}{\left|\vec{R}_{ij}\right|^3}, \tag{A2}$$

where the integral is performed along the phase *j* power line, and $d\vec{l}_j$ is the differential length vector along the phase *j* power line in the (X_j, Y_j, Z_j) coordinate system and can be found from [2]

$$d\vec{l}_j = \left[\hat{X}_j + (\cos\phi_{j,n} \frac{dY_j}{dX_j})\hat{Y}_j + (-\sin\phi_{j,n} \frac{dY_j}{dX_j})\hat{Z}_j \right] \Delta X_j, \tag{A3}$$

in which $\phi_{j,n}$ is the angular movement of the phase *j* power line while it is swinging, given in equation (2.17), and the derivative $\frac{dY_j}{dX_j}$ can be determined from geometry. Also

in equation (A2), $\vec{R}_{ij}$ is a vector from the source point in the (X_j, Y_j, Z_j) coordinate system to the observation point in the (X_i, Y_i, Z_i) coordinate system. To determine $\vec{R}_{ij}$ that involves these two coordinate systems, we must locate both the source point and the observation point in one system, by performing coordinate transformation twice. First, we use equation (2.5) to transform the location of the observation point in the (X_i, Y_i, Z_i) coordinate system to that in the common coordinate system (*x*, *y*, *z*). Then, the observation point location in the common coordinate system is transformed to that in the (X_j, Y_j, Z_j) coordinate system, making use of equation (2.4). After the coordinate system transformations, the filed point and the source point are both located in one coordinate system - the (X_j, Y_j, Z_j) system, so that the distant vector $\vec{R}_{ij}$ can be calculated. Then, substituting $d\vec{l}_j$ and $\vec{R}_{ij}$ into equation (A2) as the integrand, $\vec{B}_{ij,j}$ can be obtained by a numerical integration as shown in the appendix of [1].

Note that such obtained magnetic flux density $\vec{B}_{ij,j}$ is a vector in the (X_j, Y_j, Z_j) coordinate system and can be expressed as

$$\vec{B}_{ij,j} = B_{ijX_j}\hat{X}_j + B_{ijY_j}\hat{Y}_j + B_{ijZ_j}\hat{Z}_j . \qquad \text{(A4)}$$

To make it addable to $\vec{B}_{ii}$ in equation (A1), we must convert the vector $\vec{B}_{ij,j}$ to a vector $\vec{B}_{ij,i}$ in the (X_i, Y_i, Z_i) coordinate system. Such a conversion can be performed by using vector component transformation twice. First, we convert the vector $\vec{B}_{ij,j}$ in the

(X_j, Y_j, Z_j) coordinate system to a vector $\vec{B}_{ij,common}$ in the common coordinate system (*x*, *y*, *z*) as

$$\vec{B}_{ij,common} = B_{ijx}\hat{x} + B_{ijy}\hat{y} + B_{ijz}\hat{z}, \tag{A5}$$

in which the vector components B_{ijx}, B_{ijy}, and B_{ijz} can be found by a vector component transformation

$$\begin{bmatrix} B_{ijx} \\ B_{ijy} \\ B_{ijz} \end{bmatrix} = \begin{bmatrix} \cos\theta_j \cos\psi_j & \sin\theta_j \cos\psi_j & -\sin\psi_j \\ -\sin\theta_j & \cos\theta_j & 0 \\ \cos\theta_j \sin\psi_j & \sin\psi_j \sin\theta_j & \cos\psi_j \end{bmatrix} \begin{bmatrix} B_{ijX_j} \\ B_{ijY_j} \\ B_{ijZ_j} \end{bmatrix}. \tag{A6}$$

Then, we convert the vector $\vec{B}_{ij,common}$ in the common coordinate system (*x*, *y*, *z*) to $\vec{B}_{ij,i}$ in the (X_i, Y_i, Z_i) coordinate system as

$$\vec{B}_{ij,i} = B_{ijX_i}\hat{X}_i + B_{ijY_i}\hat{Y}_i + B_{ijZ_i}\hat{Z}_i, \tag{A7}$$

where the vector components B_{ijX_i}, B_{ijY_i}, and B_{ijZ_i} can be found by another vector component transformation

$$\begin{bmatrix} B_{ijX_i} \\ B_{ijY_i} \\ B_{ijZ_i} \end{bmatrix} = \begin{bmatrix} \cos\theta_i \cos\psi_i & -\sin\theta & \cos\theta_i \sin\psi_i \\ \sin\theta_i \cos\psi_i & \cos\theta_i & \sin\psi_i \sin\theta_i \\ -\sin\psi_i & 0 & \cos\psi_i \end{bmatrix} \begin{bmatrix} B_{ijx} \\ B_{ijy} \\ B_{ijz} \end{bmatrix}. \tag{A8}$$

Finally, substituting such calculated $\vec{B}_{ij,i}$ back into equation (A1), the total magnetic flux density $\vec{B}_i$ observed at a point on phase *i* (*i* = *a*, *b*, *c*) conductor can be obtained.

REFERENCES

[1] X.-B. Xu, X. Cheng, and K. Craven, "An analysis on magnetically induced subsequent fault in utility line topologies," *Electric Power Systems Research*, Vol. 63/3, pp. 161-168, October 2002.

[2] X.-B. Xu, Y. Yu, and K. Craven, "Magnetically induced subsequent fault in utility line topology with inclined spans," *Electric Power System Research,* Vol. 68/3, pp. 268-274, March 2004.

[3] G. Zhang, L. Tsang, and K. Pak, "Angular correlation function and scattering coefficient of electromagnetic waves scattering by a buried object under a two-dimensional rough surface," *Journal of Optical Society America, A,* vol. 15, no. 12, pp. 2995-3002, Dec. 1998.

[4] J.T. Johnson and R.J. Burkholder, "Coupled canonical grid/discrete dipole approach for computing scattering from objects above or below a rough interface," *IEEE Transactions on Geoscience and Remote Sensing*, vol. 39, pp. 1214-1220, June 2001.

[5] J.T. Johnson, "A numerical study of scattering from an object above a rough surface," *IEEE Transactions on Antennas and Propagation,* vol. 48, pp. 1361-1367, Oct. 2002.

[6] M. El-Shenawee, C. Rappaport, E. Miller, and M. Silevitch, "3-D subsurface analysis of electromagnetic scattering from penetrable/PEC objects buried under rough surface: use of the steepest descent fast multipole method (SDFMM)", *IEEE Transactions on Geoscience and Remote Sensing*, vol. 39, pp. 1174-1182, June 2001.

[7] M. El-Shenawee, C. Rappaport, and M. Silevitch, “Mote Carlo simulations of electromagnetic scattering from random rough surface with 3-D penetrable buried objects: mine detection application using the SDFMN”, *Journal of Optical Society America, A*, Dec. 2001.

[8] M. El-Shenawee, “Scattering from multiple objects buried beneath two-dimensional random rough surface using the steepest decent fast multipole method,” *IEEE Transactions on Antennas and Propagation*, vol. 51, no. 4, pp. 802-809, April 2003.

[9] J.Q. He, T.J. Yu, N. Geng, and L. Carin, “Method of moments analysis of electromagnetic scattering from a general three-dimensional dielectric target embedded in a multilayered medium,” *Radio Science*, vol. 35, no. 2, pp. 305 – 313, March-April, 2000.

[10] M. EL-Shenawee, “Polarimetric scattering from two-layered two-dimensional random rough surfaces with and without buried objects,” *IEEE Transactions on Geosciences and remote sensing*, vol. 42, no. 1, pp. 67 – 76, January 2004.

[11] C.-H Kuo and M. Moghaddam, “Electromagnetic scattering from a buried cylinder in layered media with rough interfaces,” *IEEE Transactions on Antennas and Propagation*, vol. 54, no. 8, pp. 2392 – 2401, August 2006.

[12] F.D. Hastings, J.B. Schneider, and S.L. Broschat, “A Monte-Carlo FDTD technique for rough surface scattering,” *IEEE Transactions on Antennas and Propagation*, vol. 43, no. 11, pp. 1183-1191, November 1995.

[13] L. Kuang and Y-Q Jin, “Bistatic scattering from a three-dimensional object over a randomly rough surface using the FDTD algorithm,” *IEEE Transactions on Antennas and Propagation*, vol. 55, no. 8, pp. 2302-2312, August 2007.

[14] K.H. Dridi, J.S. Hesthaven, and A. Ditkowski, "Staircase-Free finite-difference time-domain formulation for general materials in complex geometries," *IEEE Transactions on Antennas and Propagation*, vol. 49, no. 5, pp.749 – 756, May 2001

[15] G.X. Fan, Q. H. Liu, and J. S. Hesthaven, "Multidomain pseudospectral time-domain simulations of scattering by objects buried in lossy media," *IEEE Transactions on Geoscience and Remote sensing*, vol. 40, no. 6, pp. 1366 - 1373, June 2002.

[16] J.S. Hesthaven, "High-Order accurate methods in time-domain computational electromagnetics: a review," *Advances in Imaging and Electron Physics*, vol. 127, pp. 59 – 117, 2003.

[17] Y. Shi and C.-H. Liang, "A strongly well-posed PML with unsplit-field formulations in cylindrical and spherical coordinates," *Journal of Electromagnetic Waves and Applications*, vol. 19, no. 13, pp. 1761 – 1776, 2005.

[18] Primary Line Construction Customer Operations Distribution Standards, 2 ed., Duke Engergy Company 1998.

[19] H.A. Burger, "Use of Euler-rotation angles for generating antenna patterns," *IEEE Transactions on Antennas and Propagation*, vol. 37, no. 2, pp.56 – 63 April 1995

[20] T. Milligan, "More applications of Euler angles," *IEEE Transactions on Antennas and Propagation*, vol. 41, no. 4, pp.78 – 83, August 1999

[21] X.-B. Xu, H. Yang and K. Craven, "Magnetically induced swing movement of overhead power line conductors in a transition span subsequent to an initial fault," *Electrical Power System Research*, vol. 79, pp. 809-817, 2009

[22] X.-B. Xu, Y.Yu and K. Craven, "Determination of maximum span length of utility lines based on consideration of eliminating magnetically induced subsequent fault," *Electric Power Systems Research*, Vol.69, no.1, pp. 1-6, April 2004

[23] X.-B.Xu, H.Yang and K.Craven, "Magnetically induced subsequent fault (MISFault) analysis software, "*Electric Power Systems Research*, (Submitted under review)

[24] "MISFault Analysis Software Operation Guide", Presented to Duke Energy, June 2008

[25] D. Gottlieb, J.S. Hesthaven, "Spectral Methods for Hyperbolic Problems," J.Comput. Appl. Math., vol. 128, pp.83-131, 2001.

[26] G.-X. Fan, Q. H. Liu, and J.S. Hesthaven, "Multidomain pseudospectral time-domain simulations of scattering by objects buried in lossy media," *IEEE Transactions on Geoscience and Remote Sensing*, Vol. 40, No. 6, June 2002.

[27] A. Taflove and S.C. Hagness, *Computational Electrodynamics, The Finite-Difference Time-Domain Method*, Third Edition, "Chapter 17 Advances in PSTD Techniques" by Qing. Liu and Gang Zhao, Artech House, 2005.

[28] C. Canuto, M.Y Hussani, A.Quarteroni, and T. Zang, *Spectral Methods in Fluid Dynamics*, Springer-Verlag, New York, 1988.

[29] D. Gottlieb, M.Y. Hussani, and S.A. Orszag, "Theory and application of spectral methods," in *Spectral Methods for Partial Differential Equations*, Edited by R.G. Voigt, D. Gottlieb, and M.Y. Hussani, pp. 1-54, 1984.

[30] D. Gottlieb and J.S. Hesthaven, "Spectral methods for hyperbolic problems," *Journal of Computational and Applied Mathematics,* Vol. 128, Issues 1-2, pp. 83-131, March 2001.

[31] J.S. Hesthaven, "High-Order accurate methods in time-domain computational electromagnetic: a review," *Advances in Imaging and Electron Physics*, Vol. 127, pp. 59-117, 2003.

[32] S.A. Nielson and J.S. Hesthaven, "A multidomain pseudospectral formulation for the simulation of elastic wave scattering," *Journal of Acoustic Society Am*, 2001.

[33] J.P. Berenger, "A perfectly matched layer for the absorption of electromagnetic waves," *Journal of Computational Physics*, Vol. 114, pp. 185-200, 1994.

[34] W.C. Chew and W.H. Weedon, "A 3D perfectly matched medium from modified Maxwell's equation with stretched coordinates," *Microwave and Optical Technology Letters*, Vol. 7, No. 3, pp. 599-604, 1994.

[35] Q.H. Liu, "An FDTD Algorithm with perfectly matched layers for conductive media," *Microwave and Optical Technology Letters*, Vol. 14, No. 2, pp. 134-137, 1997.

[36] G.-X. Fan and Q.H. Liu, "A well-posed PML absorbing boundary condition for lossy media," *Proceedings of IEEE Antennas and Propagation Society International Symposium*, Vol. 3, pp. 2-5, 2001.

[37] G.-X. Fan and Q.H. Liu, "A strongly well-posed PML in lossy media," *IEEE Antennas and Wireless Propagation Letters*, Vol. 2, pp. 97-100, 2003.

[38] G. Zhao and Q.H. Liu, "The 3-D multidomain pseudospectral time-domain algorithm for inhomogeneous conductive media," *IEEE Transactions on Antennas and Propagation*, Vol. 52, No. 3, pp. 742 -749, March 2004.

[39] Y. Shi and C.H. Liang, "A strongly well- posed PML with unsplit-field formulation in cylindrical and spherical coordinates," *Journal of Electromagnetic Waves and Application*, Vol. 19, No. 13, pp. 1761-1776, 2005.

[40] X. Gao, M.S. Mirotznik, and D.W. Prather, "A method for introducing soft sources in the PSTD algorithm, *IEEE Transactions on Antennas and Propagation*, Vol. 52, No. 7, pp. 1665-1671, July 2004.

[41] Y. Shi, L. Li, and C.H. Liang, "Two dimensional multidomain pseudospectral time-domain algorithm based on alternating-direction implicit method," *IEEE Transactions on Antennas and Propagation*, Vol. 54, No. 4, pp. 1207-1214, April 2006.

[42] Q. Li, Y. Chen, and D. Ge, "Comparison study of the PSTD and FDTD methods for scattering analysis," *Microwave and Optical Technology Letters*, Vol. 25, No. 3, pp. 220-226, May 5 2000.

[43] X. Liu and Y. Chen, "Applications of transformed-space non-uniform PSTD (TSNU-PSTD) in scattering analysis without the use of the non-uniform FFT," *Microwave and Optical Technology Letters*, Vol. 38, No. 1, pp. 16-21, July 5 2003.

[44] M.H. Carpenter and C.A. Kennedy, "Fourth order 2N-storage Runge-Kutta schemes," *NASA Technical Memorandum 109112*, 1994.

[45] D.W. Zingg and T.T. Chrisholm, “Runge-Kutta methods for linear orfinary differential equations,” *Applied Numerical Mathematics*, Vol. 31, Issue 2, pp. 227-238, October 1999.

[46] J.S. Heathaven, P.G. Dinesen, and J.P. Lynov, “Spectral collocation time-domain modeling of diffractive optial elements,” *Journal or Computational Physics*, Vol. 155, pp. 287-306, 1999.

[47] R.F. Harrington, *Time-Harmonic Electromagnetic fields*, 2nd edition, Wiley-IEEE Press, 2001

[48] A Papoulis, *Probability, Random Variables, and Stochastic Processes*, Second Edition, McGraw-Hill Book Company, New York, 1984.

[49] P. Bill Wong, G. Leonard Tyler, and John E. Baron etc., “A Three-wave FDTD approach to surface scattering with application to remote sensing of geophysical surfaces,” *IEEE Transactions on Antennas and Propagation*, Vol. 44, No. 4, pp. 504-514, April 1996.

[50] Yun Yi, Bin Chen, Da-Gang Fang and Bi-Hua Zhou, “A new 2-D FDTD method applied to scattering by infinite object with oblique incidence,” *IEEE Transactions on Electromagnetic compatibility*, Vol. 47, No. 4, pp. 756-762, November 2005.

[51] Xianyang Zhu, Lawrence Carin, “Multiresolution time-domain analysis of plane-wave scattering from general three-dimensional surface and subsurface dielectric targets,” *IEEE Transactions on Antennas and Propagation*, Vol. 49, No. 11, pp. 1568-1578, November 2001.

[52] M.N.O. Saodiku, *Numerical Techniques in Electromagnetics*, CRC Press, 1992.

[53] M. El-Sheenawee, C. Rappaport, and M. Silevitch, "Monte Carlo simulations of electromagnetic wave scattering from a random rough surface with three-dimensional penetrable buried object: mine detection application using the steepest descent fast multiple method," *Journal of Optical Society of America*, Vol. 18, No. 12, pp. 3077-3084, December 2001.

[54] S.H. Lou, L. Tsang, C.H. Chen, and A. Ishimaru, "Monte Carlo simulations of scattering of waves by a random rough surface with the finite element method and the finite difference method," *Microwave and Optical Technology Letters*, Vol. 3, No. 5, pp. 150-154, May 1990.

[55] F.D. Hastings, J.B. Schneider, and S.L. Broschat, "A Monte-Carlo FDTD technique for rough surface scattering," *IEEE Transactions on Antennas and Propagation*, Vol. 43, No. 11, pp. 1183-1191, November 1995.

[56] R.L. Wagner, J.M. Song, and W.C. Chew, "Monte Carlo simulation of electromagnetic scattering from two-dimensional random rough surfaces," *IEEE Transactions on Antennas and Propagation*, Vol. 45, No. 2, pp. 235-245, February 1997.